SAND REPORT
SAND2002-3690
Unlimited Release
Printed November 2002

Linking the Geosciences to Emerging Bio-Engineering Technologies

Randall T. Cygan, Clifford K. Ho, and Chester J. Weiss

Prepared by
Sandia National Laboratories
Albuquerque, New Mexico 87185 and Livermore, California 94550

Sandia is a multiprogram laboratory operated by Sandia Corporation, a Lockheed Martin Company, for the United States Department of Energy under Contract DE-AC04-94AL85000.

Issued by Sandia National Laboratories, operated for the United States Department of Energy by Sandia Corporation.

Available to DOE and DOE contractors from
U.S. Department of Energy
Office of Scientific and Technical Information
P.O. Box 62
Oak Ridge, TN 37831

Telephone: (865)576-8401
Facsimile: (865)576-5728
E-Mail: reports@adonis.osti.gov
Online ordering: http://www.doe.gov/bridge

Available to the public from
U.S. Department of Commerce
National Technical Information Service
5285 Port Royal Rd
Springfield, VA 22161

Telephone: (800)553-6847
Facsimile: (703)605-6900
E-Mail: orders@ntis.fedworld.gov
Online order: http://www.ntis.gov/help/ordermethods.asp?loc=7-4-0#online

SAND2002-3690
Unlimited Release
Printed November 2002

Linking the Geosciences to Emerging Bio-Engineering Technologies

Randall T. Cygan
Geochemistry Department

Clifford K. Ho
Geohydrology Department

Chester J. Weiss
Geophysical Technology Department

Sandia National Laboratories
P.O. Box 5800
Albuquerque, New Mexico 87185-0750

Abstract

Is application of Geosciences research at Sandia National Laboratories to biological and human health systems beneficial to the lab's biotechnology efforts? This LDRD project was funded to answer that question for three application areas: biochemistry, bioengineering, and human health. The biochemistry section includes modeling for protein folding and improved drug delivery substrates. For those molecular simulations, a hybrid energy forcefield was developed to model the conformation of an oligopeptide within the clay interlayer. Results demonstrate that the nonbonded interactions are especially important in understanding the control of the structure and function of proteins as modified by inorganic substrates, and that the protein structure may be denatured by the clay surface. More sophisticated molecular simulations involving waters of solvation for the protein, hydrated clay interlayers, and different charged distributions in the clay substrates are recommended for future research. The bioengineering section focuses on drug delivery and hazardous chemical adsorption through the skin. Percutaneous absorption of chemicals was developed using a probabilistic, multiphase, heterogeneous model of the skin. Penetration routes through the skin included intercellular diffusion through the stratum corneum, diffusion through aqueous-phase sweat ducts, and diffusion through oil-phase hair follicles. Mass fluxes were calculated for varying lengths of time, and sensitivity analyses showed that the aqueous solubility limit, thickness of the stratum corneum, and aqueous molecular diffusion coefficient are important input parameters. Complex flow and transport models used for enhanced oil recovery, geothermal energy production, and subsurface contaminant migration could be used to further model percutaneous absorption. The human health section includes a review of the geophysical imaging methods that have been used for imaging the interior of the human body, electrical impedance tomography, and magnetic induction tomography. Accurate 3D interpretations of surface or near surface voltage/current or electromagnetic field measurements are dependent upon the inversion algorithms used. EIT impedance inversion is computationally less challenging than that the EM induction inversion, but rapid and resource-efficient solutions are being developed for geophysical applications. Details can be found at http://www.sandia.gov/geobio/.

Acknowledgments

This work was supported by Sandia's Laboratory Directed Research and Development (LDRD) Project 38723. Sandia is a multiprogram laboratory operated by Sandia Corporation, a Lockheed Martin Company, for the United States Department of Energy under Contract DE-AC04-94AL85000.

Table of Contents

Intentionally Left Blank

Executive Summary

Is application of geosciences research at Sandia National Laboratories to biological and human health systems beneficial to the lab's biotechnology efforts? This LDRD project was funded to answer that question for three application areas: biochemistry, bioengineering, and human health. The efforts included a comprehensive literature search and evaluation of current models and techniques to identify the state-of-the-art geoscience applications for critical areas of biotechnical research. Geoscience-based models and simulations were applied to determine their efficacy to these challenging problems.

Interactions of Biomolecules with Clay Minerals

Preliminary molecular simulations were completed to examine the intercalation of amino acids and oligopeptides in the interlayer of a clay mineral. The complex nature of biomolecules within the interlayer or on the surface of a clay mineral has significance in our fundamental understanding of such disparate topics as drug delivery systems, gene therapy, protein function, and the origin of life. The nonbonded interactions characteristic of the electrostatics and short range bonding are especially important in understanding the control of the structure and function of proteins as modified by inorganic substrates. We use a hybrid energy forcefield allowing for the simultaneous simulation of both clay and oligopeptide to determine the general behavior of various amino acid side chains within the clay interlayer. No atomic nor cell parameter constraints are imposed, thereby allowing complete constant pressure optimization and molecular dynamics with an NPT ensemble. In general, the molecular mechanics simulations suggest that clay surfaces are effective in creating significant nonbonded interactions between the clay and the oligopeptide. These interactions may be competitive with the nonbonded interactions that exist within the oligopeptide chain, and can lead to perturbation of the peptide structure once intercalated. There is evidence of denaturing of the protein structure by the clay surface in our simulations. The oligopeptide-montmorillonite example indicates the strong influence of the interlayer cations in preventing direct contact of the oligopeptide with the clay surface. The polar and charged side chains of the oligopeptide are most likely to interact with the interlayer cations. More sophisticated molecular simulations involving explicit waters of solvation for the protein, hydrated clay interlayers, and different charged distributions in the clay substrates are recommended for future research.

A Geoscience Approach to Modeling Chemical Transport through Skin

A number of similarities exist between models of percutaneous absorption and models of contaminant transport in geologic media. Both systems involve complex, multiphase, heterogeneous structures with transient diffusion and sorption of chemical species. A transient three-phase model of percutaneous absorption of chemicals has been developed in this study using a geoscience approach that includes a probabilistic multiphase heterogeneous model of the skin. Penetration routes through the skin that were modeled include the following: (1) intercellular diffusion through the stratum corneum, which was comprised of an immobile sorptive protein phase (keratinocytes) and mobile aqueous (water) and oil (lipid) phases; (2) diffusion through aqueous-phase sweat ducts; and (3) diffusion through oil-phase hair follicles. Uncertainty distributions were assigned to model parameters and a probabilistic Monte Carlo analysis was performed to simulate mass fluxes through each of the routes. Results yielded a

wide distribution of simulated mass fluxes due to the uncertainty in the input variables. At early times (60 seconds), transport through the sweat ducts provided a significant amount of mass flux into the bloodstream. At longer times (1 hour), diffusion through the stratum corneum became important because of its relatively large surface area. Similarly, diffusion through the hair follicles was more significant than diffusion through the sweat ducts at later times because of the larger porosity of hair follicles. Sensitivity analyses using stepwise linear regression were also performed to identify input parameters that were most important to the simulated mass fluxes at different times. This probabilistic analysis of percutaneous absorption (PAPA) method may prove useful to studies of exposure assessment and transdermal drug delivery.

Crossover Technologies in Geophysics and Biomedical Imaging

A common goal to both the medical and geoscience communities is the development of non-invasive methods for peering into the interior of an object. Improved biomedical imaging tools are critical to the diagnosis of numerous human diseases and organ dysfunctions. In this study, we narrow the expanse of various geophysical imaging methods by examining only those which utilize quasi-static electromagnetic fields and electrical impedance estimates for *in situ* characterization of biological structures within the human body. The problem of imaging the interior object via some non-invasive method can be broadly lumped into two primary steps: measurement of some physical quantity (such as voltage, current, or the electromagnetic fields) on the surface of the body; and utilization of an algorithm which infers the distribution of some physical property (such as electrical conductivity) within the body based solely on these surface measurements. Two imaging methods used by geophysicists for subsurface imaging have found utility as methods for imaging the interior of the human body: electrical impedance tomography and magnetic induction tomography. The principles of operation for each method are based on the observation that different biological tissues have varying capacities for sustaining a flow of electric current that is influenced by, for example, the density of vascularization in a given region. The variations in vascularization can, in some cases, be readily correlated to differences in tissue type such as lung, muscle, and bone tissues in the thorax. In other cases, the variations in the density of vascularization, and hence electrical conductivity, can be attributed to the presence of tumorous growths within the body.

1.0 General Introduction

Geosciences research at Sandia National Laboratories utilizes state-of-the-art techniques to study the fundamental science underlying complex natural physiochemical processes, often spanning time, composition, and length scales well beyond that of the materials and engineering sciences. Until recently, most of this research has been limited to applications associated with natural processes occurring within the mantle, crust, and near-surface regions of the Earth. Application of geoscience analytical, experimental, and theoretical methods to biological and human health systems would be beneficial to SNL programmatic efforts in these areas. In this effort, we have evaluated several crossover applications of the Geosciences research program at SNL to bioengineering, biochemistry, and human health areas. This work includes literature research and preliminary computer modeling to explore the potential for developing tangible links of science and technology in the biological and earth. One application area involves the chemical reactivity and binding of organic constituents, such as amino acids and oligopeptides (models for proteins), to inorganic substrates such as clay mineral surfaces. These hybrid organic-inorganic materials can be utilized in implants and drug delivery systems. A second application area examines the transport of pharmaceuticals to human individuals through the skin layers (percutaneous absorption). Concerns about the mechanisms of drug or chemical transport are critical in transdermal drug delivery and in hazardous chemical exposure assessments. The final application addressed in this study is directed at improving diagnostic imaging of soft tissue through improved interpretation of three-dimensional impedance tomographic imaging. This application is of significance in the diagnosis of cancerous growths.

At present, the research staff in the geosciences departments at SNL are leaders in the research and development of fluid flow and species transport through porous media, partitioning of chemical and molecular species between phases, sorption and reaction kinetics of chemicals in liquids and on solids, and remote electromagnetic imaging of complex multiphase structures. Geoscience-based evaluation and modeling of biological processes, diseased tissue, medical implants or pharmaceutical products could significantly augment the bioengineering and medical research and development efforts at SNL. Moreover, linking geosciences research in geochemistry, geohydrology, geomechanics, and geophysics with these biotechnical arenas complements the ongoing research in physics and computational chemistry.

This report summarizes the results of work performed in Fiscal Year 2002 to examine the feasibility of utilizing crossover technologies in the geosciences and biotechnologies for three specific biological applications. The report includes three separate sections each independently reviewing the state-of-the-art for the application. The first section reviews the computer simulations of the interactions of organic molecules on the clay mineral surfaces (Cygan), the second section discusses the modeling of three-phase percutaneous absorption processes and the application of hydrologic codes to evaluate the transport of chemicals (Ho), and the third section reviews the use of geophysical imaging methods in biomedical applications (Weiss).

2.0 Interactions of Biomolecules with Clay Minerals

Randall T. Cygan

2.1 Introduction

Almost all the dry mass of a cell is comprised of proteins. Not only do proteins constitute the building blocks from which cells are built, they are critical in executing almost every function of the cell (Alberts et al., 1998). The large number of functions is related to the different three-dimensional shapes that the proteins can adopt—specifically, structure and shape determine function. How a protein folds through the interaction of its constituent amino acids to form alpha-helixes and beta-sheets and higher order structures has only partially been determined. The ability to determine native folded state of a protein, directly from the primary sequence of amino acids is the principal goal of protein folding research. Understanding the mechanisms of protein folding, and how functional groups of the polypeptide string of amino acids interact with each other, is one of the longest-standing problems in molecular biology (King, 1993). Detailed information on the native folding state of a protein has significant impact on our understanding of biochemical pathways and their role in health disorders and disease. Improper folding and high energy configurations for proteins often result in decreased protein activity and cell disorders (Thomas et al. 1995; Taubes, 1996). The development of designer drugs, the characterization and curing of genetic diseases, and other areas of biological research that require information on protein structure and function are impacted.

Computational chemistry methods, such as molecular dynamics simulations, Monte Carlo simulations, and lattice modeling techniques, have been used to address the protein folding problem. Each method uses a similar strategy by attempting to determine the most stable, or lowest energy, conformational state for the structure of a protein (Torshin, 2001). The early-stage interactions among amino acid groups in a polymer string will ultimately control protein folding once the amino acids are condensed to form the polypeptide sequence in the ribosome of the cell. Figure 2.1 and Figure 2.2 provide graphical descriptions of an amino acid sequence and the various levels of structure associated with a protein. The number of possible interactions among amino acid functional groups is staggering and cannot be simulated in any reasonable time on the best computers, even with using the largest massively parallel computers available today. To place the computational effort into perspective, keep in mind that the typical human cell has about 10,000 different proteins with peptide sequences (residues) that vary from less than 100 amino acids to over 2200 amino acids (Alberts, et al. 1998). Therefore, several novel strategies have evolved to better sort through the number of ways in which the amino acids might be arranged into a compact folded structure. Neural network and computer training algorithms (Chang et al., 2001) and the synthesis of mini-proteins having just twenty residues (Neidigh, et al., 2001) are two recent innovations in the protein folding research.

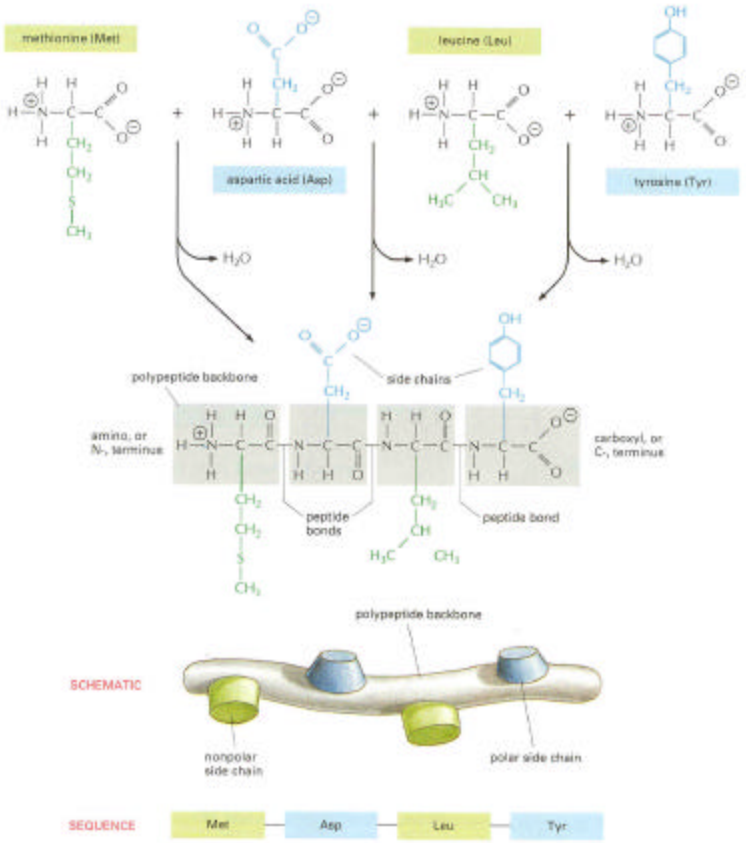

Figure 2.1. Diagram of protein (oligopeptide) formation through the condensation of amino acids (from Alberts et al., 1998).

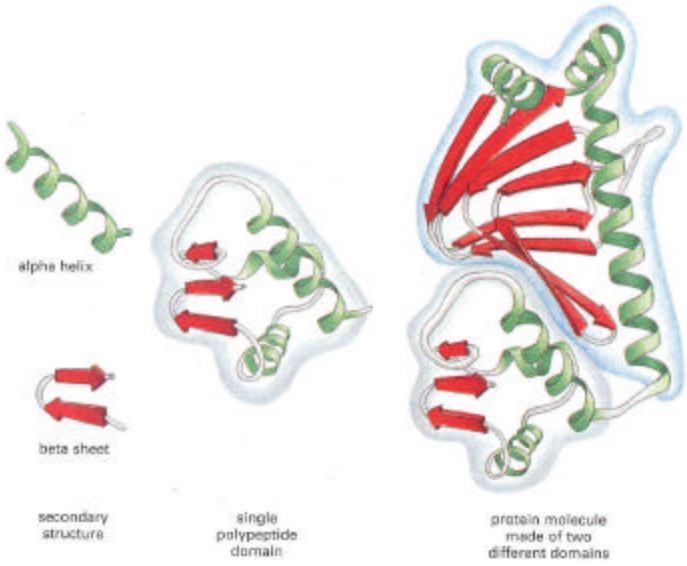

Figure 2.2. Schematic of a bacterial regulatory protein CAP showing the relationship between protein domains and other structural elements (from Alberts et al., 1998).

To date, almost the entire scientific literature on protein folding has examined the process *in vacuo* without incorporating any external influence or catalyst. Although specialized proteins referred to as molecular chaperones are used to assist in the protein folding process in the crowded cytoplasm of the cell, a protein chain can fold into the correct conformation by itself (Alberts et al., 1998). However, water solvent is omnipresent during the process and is seldom explicitly represented in molecular simulations. Additionally, catalysts in the form of substrates and surfaces are certain to modify the structure and the most stable conformations of the protein. Mineral surfaces have been suggested as providing substrates for support of the catalytic assembly of organic and biochemical molecules (Hartman; 1998; Hazen, 2001). Specifically, clay minerals and their charged aluminosilicate layered structure were envisioned as having the appropriate characteristics to harbor precursor organic molecules for the synthesis of important biomolecules.

The early studies of Cairns-Smith (1966; 1992) and Friebele et al. (1980), in particular, advocated the role of clay minerals and their surfaces as a templating unit capable of sorbing organic material (amino acids and nucleotides) from a chaotic organic-rich aqueous solution, followed by polymerization of the units to form life-critical biomolecules. Although initially considered a novel alternative origin view, this "life from rocks" theme was resurrected in the 1990's by several research groups who confirmed the intimate association of biomolecules on and in clay minerals (Pitsch et al., 1995; Violente et al., 1995; Rhode, 1999). Moreover, there was much debate on the possibility that clay interlayers and surfaces promoted the polymerization of isolated nucleotides into RNA-like compounds (Ferris, 1993; Ertem and Ferris, 1998). These heterogeneous templating reactions could have led to an increase in the possible protoncleic acids from which life ultimately emerged (Ertem and Ferris, 1996). For a more practical pharmaceutical—and less philosophical—application, recent work has shown that the double hydroxide clays (anionic clays) can incorporate DNA molecules in their interlayers and provide a suitable drug carrier for the gene therapy treatment of leukemia (Choy et al., 2000). Intercalated clays have also been shown to be effective carriers in the gastrointestinal release of selected cationic drugs (Fejer et al., 2001) including chemotherapeutic treatment of colorectal cancer (Lin et al., 2002).

Speculation on the origin of life is beyond the scope of this study, however, the ability of clay surfaces to selectively absorb biomolecules, or the monmeric and oligomeric units of these macromolecules, can be addressed. Specifically, we examine our computational capabilities to perform molecular mechanics simulations of these organic-inorganic systems based on our experience in the simulation of clay systems (Cygan et al., 1998; Hartzell et al., 1998; Cygan, 2002). Although there exists only two previous studies that used molecular modeling methods to examine the protein-amino acid-clay system, there has been no comprehensive and systematic examination of the interactions of amino acid and protein functional groups with the clay surface. Yu et al. (2000; 2001) limited their simulations to a small subset of simple proteins and oligopeptides, and used an inefficient valence forcefield that would be difficult to extend to large-scale simulations. We feel our geochemical modeling efforts, including hardware and software tools, have now matured to the point that we can critically examine these complex interactions. We present below the results of several preliminary simulations to demonstrate the ability of our own modified set of energy parameters to model these systems. A discussion of

the potential energy functions and the modifications required to introduce the organic components into the inorganic forcefield is presented next.

2.2 Potential Energy and Forcefields

The total potential energy of a chemical system is represented by the summation of the various contributing energy components:

$$E_{Total} = E_{Coul} + E_{VDW} + E_{Bond\ Stretch} + E_{Angle\ Bend} + E_{Torsion} \tag{2.1}$$

where E_{Coul}, the Coulombic energy, and E_{VDW}, the van der Waals energy, represent nonbonded energy components, and the final three terms represent the explicit bonded energy components associated with bond stretching, angle bending, and torsion dihedral, respectively. These latter terms are typically used to evaluate the energy of molecule characterized by covalent bonds, such as most organic compounds. In contrast, the energy for most inorganic materials, including halides, oxides, and silicates, is represented by the first two terms and are considered as ionic-like compounds.

The Coulombic energy, or electrostatics energy, is based on the classical description of charged particle interactions and varies inversely with the distance r_{ij}:

$$E_{Coul} = \frac{e^2}{4p e_o} \sum_{i \neq j} \frac{q_i q_j}{r_{ij}} \tag{2.2}$$

Here, q_i and q_j represents the charge of the two interacting atoms (ions), e is the electron charge, and e_o is the permittivity (dielectric constant) of a vacuum. The summation represents the need to examine all possible atom-atom interactions while avoiding duplication. Equation (2.2) will yield a negative and attractive energy when the atomic charges are of opposite sign, and a positive energy, for repulsive behavior, when the charges are of like sign. In the simple case, the Coulombic energy treats the atoms as point charges, which in practice is equivalent to spherically-symmetric rigid bodies.

Simulations involving crystalline materials or other periodic systems require the use of special mathematical methods to ensure proper convergence of the long-range nature of Equation (2.2) The $1/r$ term is nonconvergent except for the most simple and highly symmetric crystalline systems. In practice, it is therefore necessary to employ the Ewald method (Ewald 1921) or other alternative method (e.g., Greengard and Rokhlin 1987; Caillol and Levesque 1991) to obtain proper convergence and an accurate calculation of the Coulombic energy. The Ewald approach replaces the inverse distance by its Laplace transform that is decomposed into two rapidly convergent series, one in real space and one in reciprocal space (Tosi 1964; de Leeuw et al. 1980). The Coulombic energy in ionic solids typically dominates the total potential energy and, therefore, controls the structure and properties of the material. Purely ionic compounds such as the metal halide salts (e.g., NaF and KCl) are examples where the formal charge is used to accurately represent the electrostatics. In molecular systems where covalent bonding is more

common, the Coulombic energy is effectively reduced by the use of partial or effective charges for the atoms. The Coulombic energy for non-periodic systems can be evaluated by direct summation without resorting to Ewald or related periodic methods.

The van der Waals energy represents the short-range energy component associated with atomic interactions. Electronic overlap as two atoms approach each other leads to repulsion (positive energy) and is often expressed as a $1/r^{12}$ function. An attractive force (negative energy) occurs with the fluctuations in electron density on adjacent atoms. This second contribution is referred to as the London dispersion interaction and is proportional to $1/r^6$. The most common function for the combined interactions is provided by the Lennard-Jones expression:

$$E_{VDW} = \sum_{i \neq j} D_o \left[\left(\frac{R_o}{r_{ij}} \right)^{12} - 2 \left(\frac{R_o}{r_{ij}} \right)^{6} \right] \tag{2.3}$$

where D_o and R_o represent empirical parameters. Although various forms of the 12-6 potential are used in the literature, the form presented here provides a convenient expression that equates D_o to the depth of the potential energy well and R_o to the equilibrium atomic separation. This association would only apply for the interaction of uncharged atoms (e.g., inert gases), however, the functionality is used in practice for partial and full charge systems. Alternatively, a 9-6 function or a combined exponential-$1/r^6$ (Buckingham potential with three fitting parameters), among other functions, can be used to express the short-range interactions. Both 9-6 and 12-6 potential functions are incorporated into published forcefields but for the present study we incorporate the 12-6 potential. In contrast to the long-range nature of the Coulombic energy, the van der Waals energy is non-negligible at only short distances (typically less than 5 to 10 Å), and, therefore in practice, a cutoff distance is used to reduce the computational effort in the evaluation of this energy.

2.3 Hybrid Inorganic-Organic Forcefield

Various forcefield models have been used to evaluate the lattice energy of simple halides and oxides, however molecular simulations of complex inorganic compounds such as aluminosilicate phases (zeolites, ternary and higher order oxides, minerals, etc.) require a more sophisticated approach (Rappé et al., 1992; Hill and Sauer, 1994). Often these forcefields are derived empirically from experimental crystal structures, physical properties, and spectroscopic measurements. Unfortunately, these energy forcefields are often limited in their application to even more complex structures such as the environmentally important clay minerals. Recently, however, Cygan et al. (2002) developed a new forcefield that specifically addresses the molecular modeling problems associated with clay minerals. Clay minerals—characterized by large unit cells, low symmetry, complex multicomponent compositions, cation order-disorder behavior, significant vacancies, and large electrostatic potentials—and other layered phases can be successfully modeled with a fully flexible clayff forcefield. Additionally, this recent forcefield development provides an accurate description of surfaces and the behavior of water interactions. The importance of simulation methods to model these hydrated phases is critical as little structural and physical property data are available due the nanoscale of these clays and the

lack of quality single crystals available for characterization and analysis. The structure of clay minerals is characterized by a layered oxide structure comprised of tetrahedral-octahedral-tetrahedral (TOT) sheets, nominally represented by the mineral pyrophyllite with octahedral aluminum and tetrahedral silicon (Lee and Guggenheim, 1981). Isomorphic substitutions on either sheet with low-valence metal cations create a net negative layer charge that is balanced by interlayer cations, that are typically hydrated by water molecules, and which electrostatically maintain the net ionic nature of the lattice. Although other related clay structures exist, clays characterized by TOT layers having low charge are most common. This clay group includes the expandable smectite clays and is best typified by the mineral montmorillonite. Figure 2.3 provides a general description of the layered structure of the basic clay structure.

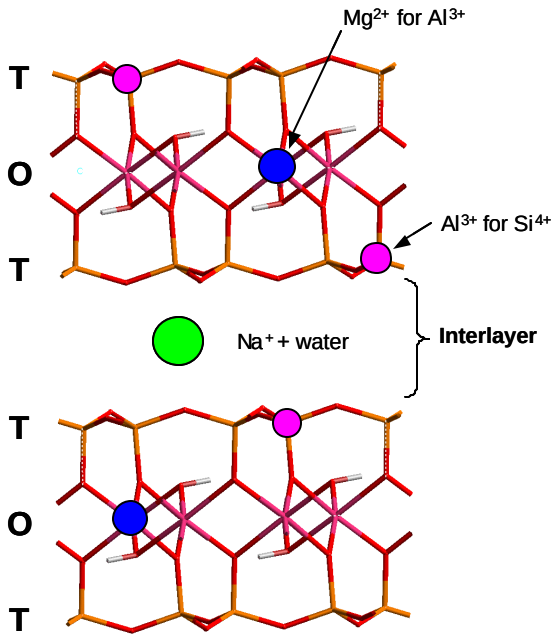

Figure 2.3 Schematic representation of 2:1 clay mineral such as montmorillonite, indicating locations of substitution sites on tetrahedral and octahedral layers and the hydrated interlayer cations.

Interatomic potentials were derived from parameterizations incorporating structural and spectroscopic data from a variety of simple hydrated compounds (Cygan et al., 2002). A flexible simple point charge (SPC) water model is used to describe the water and hydroxyl behavior (Berendsen et al., 1981; Teleman et al., 1987). Metal-oxygen interactions are described by a Lennard-Jones function (Equation 2.3) and a Coulombic term with partial charges derived by Mulliken and ESP analysis of DFT results (Equation 2.2). Bulk structures, relaxed surface structures, and intercalation processes were evaluated for several model phases and successfully compared to experimental and spectroscopic findings for validation. Of particular note is that the choice of the SPC water model is especially important for the present work due the derivation of the parameters with specific application to the simulations of protein-water interactions (Berendsen et al., 1981). An example of the success of clayff in modeling a complex clay structure and the expandability of a smectite is presented in Figure 2.4. The agreement of the simulations with the swelling behavior of montmorillonite observed by Fu et al. (1990)—

especially with the fine structure of the swelling curve as water intercalates, forms a stable hydrogen-bonded network, and rapidly expands the clay TOT layers—provides significant validation for the use of clayff in modeling clay intercalation processes.

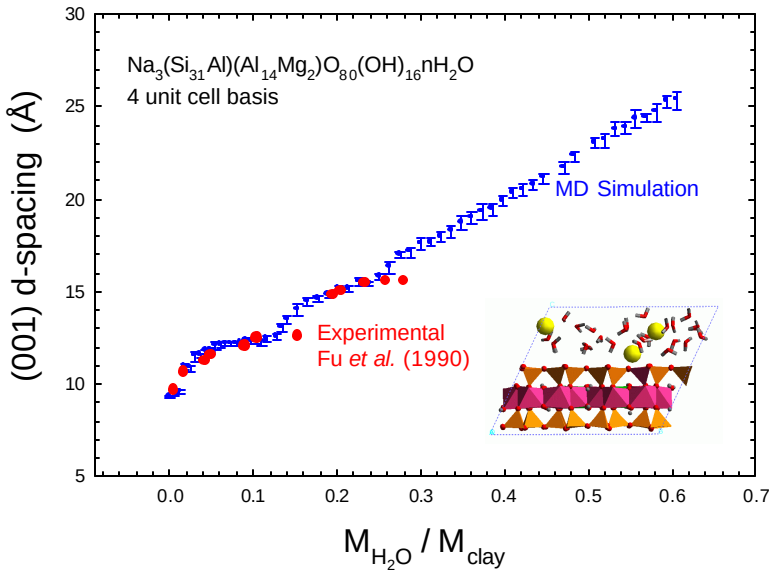

Figure 2.4 Swelling behavior for a smectite clay derived from molecular dynamics simulations. Expansion of clay interlayer with increasing water content is denoted directly by X-ray diffraction measurement of the basal (001) d-spacing.

For the molecular simulation of biomolecules interacting with clay surfaces, we desired an accurate and relatively simple energy forcefield that was compatible with the functionality represented in clayff, and which accurately modeled amino acids and protein structures. Moreover, it was important that the organic forcefield parameters be readily incorporated into clayff using the same energy software. We ultimately chose the organic CVFF forcefield (consistent valence forcefield; Dauber-Osguthorpe, et al. 1988) for integration with clayff. This hybrid forcefield has been successfully tested for several cases where simple organic compounds (hydrazine, trichloroethylene, tributylphosphate, etc.) have been introduced into the interlayer of smectite clays. However, this study presents the first simulations for the analysis of amino acids and other biomolecules within clays using the combined clayff-CVFF forcefields, and now referred to as clayoff.

2.4 Simulation Procedure

All molecular simulations were carried out using the Cerius2 software package (Accelrys Inc., San Diego) and the OFF energy algorithm. The bulk of the modeling effort was devoted to testing the compatibility of the new clayoff forcefield for the hybrid cells. Energy minimization and molecular dynamics simulations were performed in this preliminary analysis of intercalated biomolecules within the clay. Large periodic simulation cells were created from previously optimized montmorillonite structures. These cells were expanded and the bimolecular was inserted into the interlayer. Preliminary simulations avoided the introduction of water within the

interlayer, however, interlayer Na^+ cations were introduced appropriately to balance the negative clay layer charge. Energy optimizations were performed allowing all atomic positions and cell parameters to vary during the minimization process, thereby simulating a system under constant pressure conditions. Several representative amino acids for intercalation were chosen in this analysis. These include representative acids having a polar, nonpolar, charged, and charged side chains: methionine, aspartic acid, leucine, and tyrosine. This amino acid sequence, referred to as an oligopeptide, is graphically presented in Figure 2.1. The individual amino acids were first created through appropriate software tools and then clayoff parameters and partial charges were assigned. Each amino acid was energy optimized to obtain the lowest energy configuration. These structures were then combined or linked together to create the representative oligopeptide that was then subjected to an energy minimization procedure. Amino and carboxylate groups are protonated and deprotonated, respectively, to represent the pH environment expected within the cytoplasm of a cell. Once fully optimized, the oligopeptide structure was then incorporated into the clay for subsequent optimization. No effort was made to examine the role of the optical activity of the central carbon of the amino acid in this preliminary study; all proteins are comprised exclusively of L-amino acids (left-handed chirality).

2.5 Results

The results of the energy optimization for the isolated oligopeptide are presented in Figure 2.5. The structure of this mini-protein exhibits one of the stable complex conformations that can occur with the disposition of the various amino acid side chains away from the central polypeptide backbone. Nonpolar side chains such as methionine and leucine are typically directed away from the backbone and lead to congregation of similar groups at the internal fold of a protein. Typically for larger protein structures the nonpolar side chains groups occur in the core region of the protein to create a hydrophobic region. In contrast, the more polar or charged groups have more interactions with each other and with solvating water molecules. These groups are typically orient themselves on the outside of the folded protein molecule and form a relatively strong hydrogen bond network. The oligopeptide presented here shows the strong interaction of the hydroxyl of the phenol group of tyrosine with the charged carboxylate of aspartate side chain resulting in a slight fold of the polypeptide backbone. Although this result is on a small scale, the example represents the concerted efforts of larger sequences of amino acids in proteins that control complex protein folding.

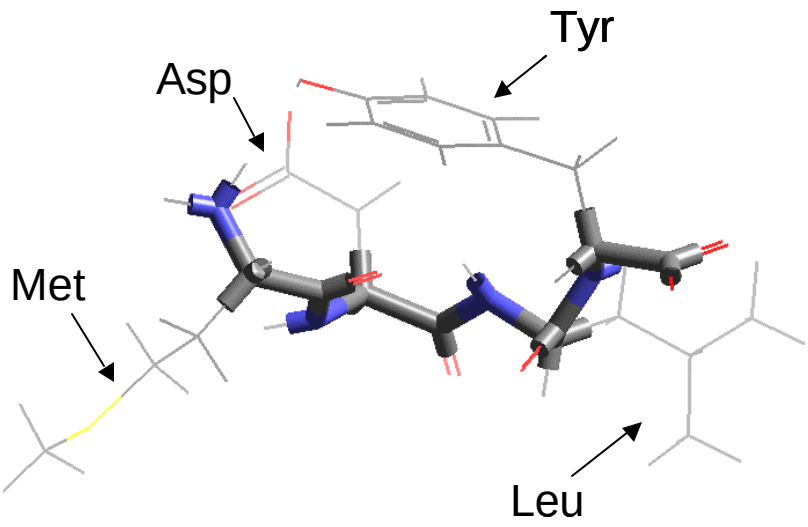

Figure 2.5. Geometry optimized conformation of the test oligopeptide comprised of methionine (Met), aspartic acid (Asp), leucine (Leu), and tyrosine (Tyr). The polypeptide backbone comprised of sequential amino-hydrocarbon-carboxyl groups is highlighted.

Once intercalated within the interlayer of the clay, the molecular modeling results indicate a slightly different conformation for the oligopeptide. A montmorillonite clay having a layer charge of -0.75 per $O_{20}(OH)_4$ unit and sodium interlayer cations is used in the simulation. An additional interlayer cation is required to balance the negative charge associated with the aspartate side group of the oligopeptide and maintain a neutral simulation cell. The use of the clayoff forcefield allows complete flexibility for all atoms and cell parameters during the simulation. Most of the layer charge is balanced by the interlayer cations being sorbed directly onto the siloxane surfaces on either side of the oligopeptide. The tyrosine and aspartate groups remain coordinated to each other within the clay and the nonpolar methionine and leucine side chains are now more disposed subparallel to the clay layers. The terminal carboxylate group of the peptide chain is now interacting with one of the interlayer cations. Analysis of the view normal to the clay interlayer (not shown) indicates the oligopeptide structure to be more two-dimensional (flattened) relative to the isolated gas-phase calculation. This may be evidence of a denaturing process associated with clay intercalation and was similarly observed in the simulations of Yu et al. (2000).

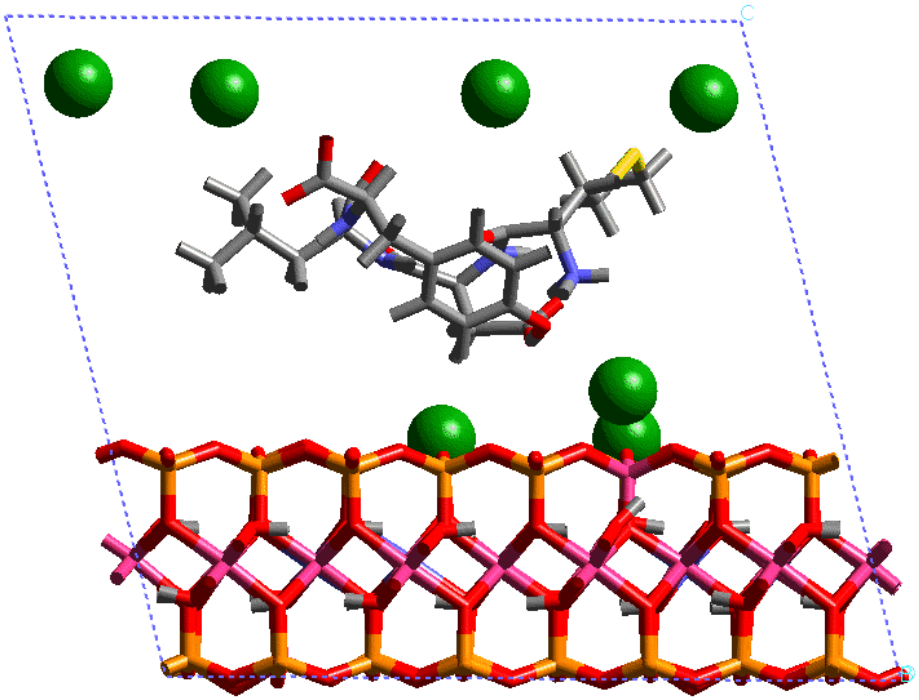

Figure 2.6 Geometry optimized arrangement of the oligopeptide within the interlayer of a montmorillonite clay; (010) view. The green spheres represent interlayer sodium cations required to balance the charge of the clay layer and oligopeptide. All atoms and cell parameters were allowed to vary during the simulation.

The montmorillonite substrate maintains the expected clay structure after intercalation but now exhibits an expanded cell with a basal d-spacing of 18.6 Å compared to the 9.2 Å without the intercalate or water. There is some deflection of the inner hydroxyl groups associated with the sorbed sodium ions but most remain subparallel to the clay layer. The sodiums are most likely to sorb at the aluminum tetrahedral site due to the localized charge directly at the layer surface.

A related set of calculations examined the behavior the identical oligopeptide within the interlayer of pyrophyllite clay. Pyrophyllite, $Al_2Si_4O_{10}(OH)_2$, possesses no tetrahedral or octahedral substitutions and, with no layer charge, does not require charge-compensating interlayer cations. A background screening term to provide a neutral cell compensated the excess charge on the oligopeptide. No constraints were imposed allowing all atoms and cell parameters to vary during the simulation. The fully-optimized configuration is presented in Figure 2.7. Without the interlayer cations, the oligopeptide has more freedom to directly interact with the siloxane surfaces of the pyrophyllite. The oligopeptide is stabilized in a conformation that is similar to that observed for montmorillonite but with more interaction of the hydrocarbon groups and the methionine side chain with the clay surface. There is minor relaxation of the siloxane surface in response to these interactions. The basal d-spacing increases from 9.1 Å to 16.2 Å with the intercalate, which is slightly compressed relative to the d-spacing obtained for the intercalated montmorillonite. The lack of local charge on the pyrophyllite surface is less effective in controlling the localized interactions between the oligopeptide and the clay.

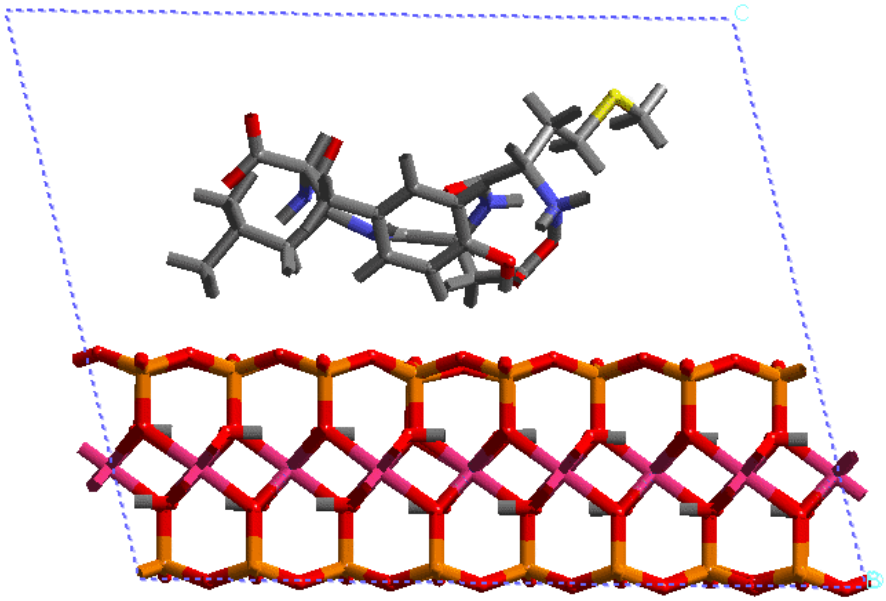

Figure 2.7 Geometry optimized arrangement of the oligopeptide within the interlayer of a pyrophyllite clay; (010) view. Pyrophyllite has no layer charge and no interlayer cations. All atoms and cell parameters were allowed to vary during the simulation.

Several molecular dynamics calculations for the clay-oligopeptide system were performed for simulation times up to 40 ps as an NPT canonical ensemble. In general, the results support the optimized structure presented in Figures 2.6 and 2.7 These preliminary dynamics simulations were performed primarily as test cases to determine the behavior of the clayoff forcefield for the hybrid systems and to determine the computational limits on the simulation cell size, number of atoms, time steps, and frequency of trajectory storage.

2.6 Conclusions

In general, the molecular mechanics simulations suggest that clay surfaces are effective in creating significant nonbonded interactions between the clay and the oligopeptide. These interactions may be competitive with the nonbonded interactions within the oligopeptide chain, and can lead to perturbation of the peptide structure once intercalated. There is some evidence of denaturing of the protein structure by the clay surface in our simulations. The oligopeptide-montmorillonite example indicates the strong influence of the interlayer cations in preventing direct contact of the oligopeptide with the clay surface. The polar and charged side chains of the peptide are most likely to interact with the interlayer cations.

Future research of these peptide-clay systems would benefit by completing a series of simulations on oligopeptides with various amino acids—basic, acidic, nonpolar, and polar side chains—in order to best categorize the general behavior of each group with the clay substrate. Additionally, it would be important to examine the role of explicit water molecules in the solvation of the protein and the influence of water in the clay interlayer. The complex

competition among processes involving water solvation of the protein, the formation of hydrogen bonded water network, and the structured layering of water on the clay surfaces will ultimately influence the protein structure. The clayoff forcefield already incorporates the flexible SPC water model that accurate predicts structure and energy behavior that could be used in this effort. It is critical to examine layer charge and charge distribution by simulating a variety of clay structures, especially comparing those with charge distributed locally on the tetrahedral sheet (beidellite), octahedral sheet (montmorillonite), and with no charge (pyrophyllite). As a final thought, it is conceivable that perhaps ordering of the isomorphic substitutions (Al^{3+} for Si^{4+}) in the tetrahedral sheet of a beidellite clay may be responsible for the templating of selected amino acids and that the clay surface catalyzes their condensation to form the first proteins. Molecular simulations may provide the critical tool to test this critical hypothesis.

2.7 References

Alberts, B., Bray, D., Johnson, A., Lewis, J., Raff, M., Roberts, K., and Walter, P. (1998) *Essential Cell Biology*, Garland Publishing, Inc., New York.

Berendsen, H.J.C., Postma, J.P.M., van Gunsteren, W.F., and Hermans, J. (1981) Interaction models for water in relation to protein hydration. In B. Pullman, Ed. *Intermolecular Forces*, p. 331- 342. D. Reidel.

Caillol, J.M. and Levesque, D. (1991) Numerical simulations of homogeneous and inhomogeneous ionic systems: An efficient alternative to the Ewald method. *Journal of Chemical Physics*, 94(1), 597-607.

Cairns-Smith, A. G. (1966) The origin of life and the nature of the primitive gene. *Journal of Theoretical Biology*, 10, 53-88.

Cairns-Smith, A. G., Hall, A. J., and Russell, M. J. (1992) Mineral theories of the origin of lifeand an iron sulfide example. *Orignin of Life and Evolution of the Biosphere*, 22, 161-180.

Chang, I., Cieplak, M., Dima, R. I., Maritan, A., and Banavar, J. R. (2001) Protein threading by learning. *Proceedings of the National Academy of Sciences*, 98, 14350-14355.

Choy, J. H., Park, J. S., Kwak, S. Y., Jeong, Y. J., and Han, Y. S. (2000) Layered double hydroxide as gene reservoir. *Molecular Crystals and Liquid Crystals*, 341, 1229-1233.

Cygan, R.T. (2002) Molecular models of radionuclide interaction with soil minerals. In P. Zhang, and P.V. Brady, Eds. *Geochemistry of Soil Radionuclides*, p. 87-109. Soil Science Society of America, Madison.

Cygan, R. T., Nagy, K. L., and Brady, P. V. (1998) Molecular models of cesium sorption on kaolinite. In E.A. Jenne, Ed. *Adsorption of Metals by Geomedia*, p. 383-399. Academic Press, New York.

Cygan, R.T., Liang, J.-J., and Kalinichev, A.G. (2002) Molecular models of hydroxide, oxyhydroxide, and clay phases and the development of a general forcefield. *Journal of Physical Chemistry*, submitted.

Dauber-Osguthorpe, P., Roberts, V.A., Osguthorpe, D.J., Wolff, J., Genest, M., and Hagler, A.T. (1988) Structure and energetics of ligand-binding to proteins: Escherichia-coli dihydrofolate reductase trimethoprim, a drug-receptor system. *Proteins: Structure, Function, and Genetics*, 4(1), 31-47.

de Leeuw, S.W., Perram, J.W., and Smith, E.R. (1980) Simulation of electrostatic systems in periodic boundary conditions: 1. Lattice sums and dielectric constants. *Proceedings of the Royal Society of London, Series A: Mathematical and Physical Sciences*, 373(1752), 27-56.

Ertem, G. and Ferris, J. P. (1996) Synthesis of RNA oligomers on heterogeneous templates. *Nature*, 379, 238-240.

Ertem, G. and Ferris, J. P. (1998) Formation of RNA oliogomers on montmorillonite: Site of catalysis. *Origins of Life and Evolution of the Biosphere*, 28, 485-499.

Ewald, P.P. (1921) Die Berechnung optishcer und elektrostatischer Gitterpotentiale. *Annalen der Physick*, 64, 253-287.

Fejer, I., Kata, M., Eros, I., Berkesi, O., and Dekany, I. (2001) Release of cationic drugs from loaded clay minerals. *Colloid and Polymer Science*, 279, 1177-1182.

Ferris, J. P. (1993) Catalysis and prebiotic RNA synthesis. *Origins of Life and Evolution of the Biosphere*, 23, 307-315.

Friebele, E., Shimoyama, A., and Ponnamperuma, C. (1980) Adsorption of protein and non-protein amino acids on a clay mineral: A possible role of election in chemical evolution. *Journal of Molecular Evolution*, 269-278.

Fu, M.H., Zhang, Z.Z., and Low, P.F. (1990) Changes in the properties of a montmorillonite-water system during the adsorption and desorption of water: Hysteresis. *Clays and Clay Minerals*, 38(5), 485-492.

Greengard, L. and Rokhlin, V. (1987) A fast algorithm for particle simulations. *Journal of Computational Physics*, 73(2), 325-348.

Hartman, H. (1998) Photosynthesis and the origin of life. *Origins of Life and Evolution of the Biosphere*, 28, 515-521.

Hartzell, C. J., Cygan, R. T., and Nagy, K. L. (1998) Molecular modeling of the tributyl phosphate complex of europium nitrate in the clay hectorite. *Journal of Physical Chemistry A*, 102, 6722-6729.

Hazen, R.M. (2001) Life's rocky start. *Scientific American*, April, 77-85.

Hill, J.R. and Sauer, J. (1994) Molecular mechanics potential for silica and zeolite catalysts based on ab initio calculations: 1. Dense and microporous silica. *Journal of Physical Chemistry*, 98(4), 1238-1244.

King, J. (1993) The unfolding puzzle of protein folding. *Technology Review*, 58-61.

Lee, J.H. and Guggenheim, S. (1981) Single crystal X-ray refinement of pyrophyllite-1Tc. *American Mineralogist*, 66(3-4), 350-357.

Lin, F. H., Lee, Y. H., Wong, J. M., Shieh, M. J., and Wang, C. Y. (2002) A study of purified montmorillonite intercalated with 5-fluorouracil as drug carrier. *Biomaterials*, 23, 1981-1987.

Neidigh, J. W., Fesinmeyer, R. M., and Andersen, N. H. (2001) Designing a 20-residue protein. *Nature Structural Biology*, 9, 425-430.

Pitsch, S., Eschenmoser, A., Gedulin, B., Hui, S., and Arrhenius, G. (1995) Mineral induced formation of sugar phosphates: Chemistry of alpha-montmorillonite from the Zurich group. *Origins of Life and Evolution of the Biosphere*, 25, 297-334.

Rappé, A.K., Casewit, C.J., Colwell, K.S., Goddard, W.A., and Skiff, W.M. (1992) UFF, a full periodic table force field for molecular mechanics and molecular dynamics simulations. *Journal of the American Chemical Society*, 114, 10024-10035.

Rode, B. M. (1999) Peptide and the origin of life. *Peptides*, 20, 773-786.

Taubes, G. (1996) Misfolding the way to disease, *Science*, 271**,** 1493-1495.

Teleman, O., Jonsson, B., and Engstrom, S. (1987) A molecular dynamics simulation of a water model with intramolecular degrees of freedom. *Molecular Physics*, 60, 193-203.

Thomas, P. J., Qu, B.-H., and Pedersen, P. L. (1995) Defective protein folding as a basis of human disease, *Trends in Biochemical Sciences*, 20, 456-459

Torshin, I. Y. (2001) Clustering amino acid contents of protein domains: Biochemical functions of proteins and implications for origin of biological macromolecules. *Frontiers in Bioscience*, 6, A1-A12.

Tosi, M.P. (1964) Cohesion of ionic solids in the Born model. *Solid State Physics*, 131, 533-545.

Violante, A. de Cristofaro, A., Rao, M. A., and Gianfreda, L. (1995) Physicochemical properties of protein-smectite and protein-$Al(OH)_x$-smectite complexes. *Clay Minerals*, 30, 325-336.

Yu, C.H., Norman, M.A., Newton, S.Q., Miller, D.M., Teppen, B.J., and Schäfer, L. (2000) Molecular dynamics simulations of the adsorption of proteins on clay mineral surfaces. *Journal of Molecular Structure*, 556, 95-103.

Yu, C.H., Newton, S.Q., Miller, D.M., Teppen, B.J., and Schäfer, L. (2001) Ab initio study of the nonequivalence of adsorption of D- and L-peptides on clay mineral surfaces. *Structural Chemistry*, 12, 393-398.

3.0 A Geoscience Approach to Modeling Chemical Transport through Skin

Clifford K. Ho

3.1 Introduction

Modeling chemical transport through human skin (percutaneous absorption) serves an important role in two primary arenas: (1) hazardous chemical-exposure assessments and (2) transdermal drug delivery. In the former, models are used to understand relevant features and processes of percutaneous absorption so that protective measures can be designed and implemented that minimize the risk of dermal absorption of toxic chemicals (Stewart and Dodd, 1964; Bird, 1981; Flynn, 1990; EPA, 1992; Ness, 1994; Poet et al., 2000; McDougal and Boeniger, 2002; Poet and McDougal, 2002). In the latter arena, researchers are striving to enhance the viability of transdermal delivery of drugs such as analgesics, insulin, and more recently, peptides and proteins (Amsden and Goosen, 1995; Potts and Guy, 1995; Kalia and Guy, 2001). Transdermal delivery of drugs that require low dosages for long periods can be more effective, less costly, and less painful than traditional alternatives such as injection, intravenous infusion, or oral ingestion.

Developing accurate and reliable models of chemical transport through the skin can yield information regarding the important features and processes that contribute to the retardation or enhancement of chemical permeation. Many of the models that have been considered previously have focused on steady-state Fickian diffusion through the skin (Michaels et al., 1975; Flynn, 1990). Transient models have been developed (Scheuplein, 1967; Kalia and Guy, 2001), but simplifying assumptions were made so that analytical solutions could be obtained. In addition, boundary conditions and properties were stylized according to the field of application (either for exposure assessment or drug delivery). For example, models used for exposure assessments typically focus on industrial solvents and other hydrocarbons (e.g., trichloroethylene), which are generally lipophilic and hydrophobic. On the other hand, models used in drug-delivery studies often focus on hydrophilic solutes (i.e., drugs that dissolve in water). These considerations impact the boundary conditions of the models, as well as the choice of partitioning coefficients and the layers of skin that are included in the models. The application-specific models make it difficult to draw general conclusions regarding the features and processes that most affect the permeability of particular solutes and solvents. In addition, models are often used with deterministic property values, which do not consider the large uncertainty inherent in biological systems and properties.

A number of similarities exist between models of percutaneous absorption and models of contaminant transport in geologic media. Both systems involve complex, multiphase, heterogeneous structures with transient diffusion and sorption of chemical species. Models of contaminant transport in fractured rock also simulate features (e.g., fractures) that may create "fast-flow" paths within a larger continuum. This is analogous to hair follicles and sweat glands that penetrate the skin, potentially creating shunts for chemical transport through the skin. In addition, probabilistic methods have been developed for performance assessments of complex transport processes in geologic structures to quantify risk and uncertainty and to perform sensitivity analyses (DOE, 1998). These methods can be applied to models of percutaneous absorption to perform similar assessments.

The purpose of this work is to review previous models of percutaneous transport and to identify important assumptions and issues relevant to each model. A stochastic analysis adopted from contaminant transport models of geologic media is then applied to models of percutaneous absorption. In particular, a mechanistic model of transient percutaneous absorption will be developed that is used in conjunction with probabilistic methods to estimate probability distributions for permeation and chemical dose. Uncertainty distributions for model-input parameters are developed, and a Monte Carlo analysis is performed using the mechanistic model to quantify the impacts of the uncertainties on the simulated results. Sensitivity analyses are also performed to identify the parameters that are most important to the simulated results. A review of the anatomy of the skin and the factors that are likely to impact chemical permeation are provided first, followed by a description and discussion of the models and results.

3.2 Anatomy of the Skin

The skin is a complex organ that serves to protect humans from chemical, physical, and biological intrusion, while retaining moisture and providing thermal regulation. It consists of three primary regions: the epidermis, the dermis, and the hypodermis (see Figure 3.1). The epidermis is the outermost layer of the skin in contact with the environment, ranging between 0.075 and 0.20 mm thick in most regions and between 0.4 and 0.6 mm thick in the palms and soles (Amsden and Goosen, 1995; Flynn, 1990). It consists of the stratum corneum, which forms the outermost layer of the epidermis, and the viable epidermis, which consists of the granular, spinous, and basal layers. The epidermis does not contain any capillary vasculature, so chemicals that transport through the epidermis must also transport partially through the dermis to reach the bloodstream. The cells in the epidermis are continually shed to the surface and replaced from the basal layer. These cells are replaced completely on the average of once every two weeks.

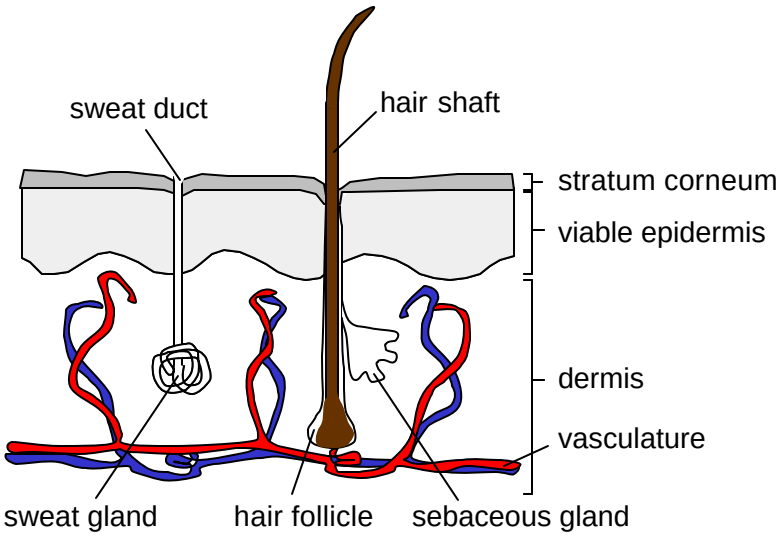

Figure 3.1 Skin features relevant to percutaneous absorption of chemicals.

The outermost layer of the epidermis, the stratum corneum, is the primary barrier to permeation of most drugs and chemicals (Scheuplein, 1976; Michaels et al., 1975). The stratum corneum is between 10 and 50 μm thick (15-20 cell layers thick) and contains dead keratinized cells (keratinocytes) with lipid lamellae filling the intercellular regions. It is composed of a very heterogeneous structure containing approximately 20-40% water, 20% lipids, and 40% keratinized protein. The keratinocytes, connected together in a planar array by desmosomes, are thin platelets filled with polar protein strands woven into compact and dense keratin fibers. The lipids form a continuous, albeit extremely tortuous, intercellular network between the keratinocytes. The compactness of the keratinocytes and the limited amount of intercellular lipid results in the low permeability of the stratum corneum.

The underlying dermis contains the vasculature (blood vessels and lymph vessels) that can uptake chemicals diffusing through the skin. The vasculature can reach to within a few microns of the undersurface of the epidermis. The dermis consists of a moderately dense network of connective tissue composed of collagen fibers and elastic fibers. It varies in thickness from 1 to 4 mm depending on the location of the body. Diffusion through this layer is analogous to diffusion through hydrogels (Amsden and Goosen, 1995).

Hair follicles and sweat glands, called skin appendages, break the continuity of the epidermal and dermal layers throughout most of the surface of the body. On average, 40 to 100 hair follicles and 210 to 220 sweat ducts exist per square centimeter of skin, occupying about 0.1% of the total surface area (Scheuplein, 1967). Hair follicles extend through the epidermis into the dermis, where the base of the follicle is well vascularized. Sebaceous glands attached to the sides of the follicles secrete sebum, a lipid mixture, into the region between the hair and the sheath. The sweat glands consist of tubes extending from the dermis, where the tube is coiled and vascularized, to the skin surface where a watery mixture (sweat) is excreted to provide thermal regulation.

3.3 Skin Permeation Routes and Previous Models

Based on the physiology of the skin, three possible pathways exist for passive transport of chemicals through the skin to the vascular network (Scheuplein, 1965; Scheuplein and Blank, 1971): (1) intercellular diffusion through the lipid lamellae; (2) transcellular diffusion through both the keratinocytes and lipid lamellae; and (3) diffusion through appendages (hair follicles and sweat ducts). Figure 3.2 illustrates these potential pathways.

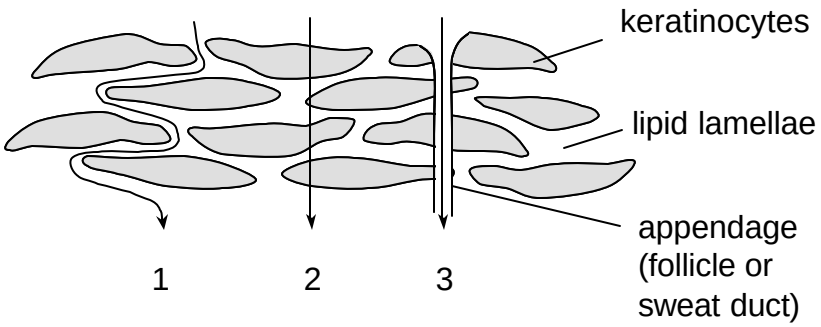

Figure 3.2 Skin permeation routes through the stratum corneum: (1) intercellular diffusion through the lipid lamellae; (2) transcellular diffusion through both the keratinocytes and lipid lamellae; and (3) diffusion through appendages (hair follicles and sweat ducts).

A number of models have been developed that simulate one or more of these pathways. Michaels et al. (1975) considered the first two modes of transport by modeling the steady-state behavior of the stratum corneum as a two-phase "brick and mortar" region (the aqueous protein phase in the keratinocytes was modeled as the bricks and the intercellular lipid phase was modeled as a continuous mortar). They assumed that the transport was the sum of steady diffusion (1) through the lipid and protein in series and (2) through the lipid phase via a tortuous path. They estimated tortuosities (~10:1) and diffusion coefficients through the lipid and protein. Experiments were conducted using cadaver skins and several different drug chemicals. Results showed a permeation dependence on pH (higher pH gave a higher flux for the same concentration) and mineral oil/water partition coefficient (larger partition coefficients yielded greater fluxes). They concluded that the ratio of the lipid diffusivity to the protein diffusivity (one of the two important parameters in their model) was 10^{-2} to 10^{-3}, meaning that the diffusion coefficient for the lipid phase was about 500 times less than the diffusion coefficient for the protein phase, which they estimated to be about 2×10^{-7} cm^2/s (from Michaels et al., 1975).

Flynn (1990), however, stated that the density and compactness of the intracellular protein in the keratinocytes of the stratum corneum presents a thermodynamically and kinetically impossible passageway for chemical transport. Other recent investigators also supported the belief that when comparing evidence for intercellular versus transcellular diffusion, intercellular diffusion through the lipid lamellae is the predominant mode of transport (Amsden and Goosen, 1995). As a result, Flynn (1990) proposed an alternate "aqueous pore pathway" in parallel (as opposed to in series) with the lipid pathways through the stratum corneum to represent the limited intercellular aqueous phase. Although the location of these aqueous pathways was uncertain, Flynn included these pathways to accommodate the diffusion of polar compounds. Other researchers have argued a similar phenomenon by considering both a polar and non-polar pathway through the stratum corneum. Elias (1981) described the polar pathway in terms of aqueous pores in the small aqueous phase between the lipid lamellae. Supporting this theory, Cooper (1984) found that polar molecules such as water and small ions permeated the skin and that the flux was independent of the oil/water partition coefficient. As the polarity of the molecules decreased, the flux became a function of the partition coefficient (Scheuplein and Blank, 1971).

Results of Flynn (1990) showed that diffusion was a direct function of the octanol/water partition coefficient, K_{ow}, and molecular weight, *MW* (for a given K_{ow}, chemicals with larger molecular weights exhibited lower diffusion; for a given *MW*, chemicals with greater K_{ow} yielded more diffusion). The study showed that larger molecular-weight chemicals permeated slower in general, but the phase of the vehicle (water or oil) delivering the chemical was not specified. Scheuplein (1976) and Potts and Guy (1995) point out that the permeability of a chemical depends on the phase of the vehicle. If the molecular weight is high, indicating a more lipophilic compound, then the permeability will be greater if the vehicle is a water than an oil since the compound will want to partition out of the water and into the tissue. Flynn (1990) also presented a simple exposure-assessment equation using the results of his modeling that expressed the cumulative mass entering the skin. The permeability coefficient was determined from simple equations that were correlated to experimental results for different K_{ow} and *MW* values. The equation assumed that the cumulative mass entering the skin took place after the lag time, which Flynn estimated could be approximately 10 minutes for MW<150 and 1 hour for MW>150.

Scheuplein (1967) developed analytical transient models of percutaneous absorption considering transport via appendages. He compared transport through appendages with transport through the intact stratum corneum, which he modeled as two single-phase regions: (1) the stratum corneum with a thickness of 10 µm and (2) the aqueous viable epidermis and papillary dermis with a combined thickness of 200 µm. To determine the cumulative amount of chemical transported, he used a composite slab solution (using resistances in series). From this he concluded that the appendages (follicles and sweat ducts), which had several orders of magnitude higher diffusion coefficients, allowed greater transport at early times, but that the bulk stratum corneum would allow greater diffusion at longer times. To determine concentrations profiles, he used a steady-state solution to determine the steady concentrations in the two slabs and a semi-infinite solution to determine the transient concentrations in the two slabs. The semi-infinite solution does not yield a concentration of zero at the boundary of the basal layer, which was inconsistent with his general formulation, but it did provide some relative comparisons. He also showed that the partitioning coefficient between the lipid and aqueous regions could also impact the concentration gradient.

Kalia and Guy (2001) developed a number of analytical solutions for transient diffusion of drugs through the skin. They treated the skin as a homogeneous slab, but they considered different scenarios for the delivery vehicle (e.g., patch with a reservoir on top, patch with drug dispersed, drug in an ointment, etc.). They concluded that a unified model that could consider the effects of molecular weight and partition coefficients was necessary.

Other models have been developed that do not consider the specific routes of transport through the skin but attempt to describe the general rate of chemical transport through the skin and/or into the circulatory system using empirical observations and lumped-capacitance models. These models are generally described as physiologically-based pharmaco-kinetic models (PBPK). The general method is to correlate existing data to simple compartment models that represent the skin and various processes and regions associated with uptake into the body. Potts and Guy (1995) and Poet et al. (2000) have developed PBPK models that can predict chemical diffusion and uptake through the skin using physical properties of the chemical. Potts and Guy (1995) developed a model that provides an algorithm to predict permeability from the drug's physical

properties. Multiple regression analyses were performed using previous data of the permeability coefficient for different chemicals, and the molecular volume and the hydrogen bond activity parameters were determined to be important. However, this model is only valid when the stratum corneum is the rate-limiting barrier to percutaneous absorption (i.e., for polar compounds). Poet et al. (2000) used a PBPK model to estimate skin permeability values and to predict exhaled concentrations of trichloroethylene (TCE) when subjects were exposed to TCE. Good agreement was obtained between predicted and observed TCE concentrations, but the relative importance of the various features and processes were not elucidated. In general, specific routes of permeation that contribute to the overall rate of transport through skin are not considered in PBPK models.

3.4 Model Development

Most of the models of percutaneous absorption that have been developed previously treat the skin as a homogeneous medium with an effective (average) permeability coefficient. These include many of the transient analyses (e.g., Kalia and Guy, 2001) and the PBPK analyses (e.g., Poet et al., 2000). A few models that do consider multiphase heterogeneous transport through the various layers and pathways of the skin often assume steady-state conditions (e.g., Michaels et al., 1975; Flynn, 1990). Scheuplein (1967) developed models of transient diffusion through different pathways in the skin, but deterministic models were used. In the following sections we develop a probabilistic, transient, multiphase model of chemical transport through various routes in the skin to address the inherent uncertainties in the processes and parameters associated with percutaneous absorption.

In particular, we consider the following possible pathways: (1) intercellular diffusion through the lipids and aqueous "pores" in the stratum corneum (pathway #1 in Figure 3.2); and (2) diffusion through appendages (hair follicles and sweat ducts) (pathway #3 in Figure 3.2). We do not consider the transcellular pathway across keratinocytes and lipids (pathway #2 in Figure 3.2) because the evidence presented earlier suggests that diffusion through the keratinocytes would be extremely small.

3.4.1 Intercellular Diffusion through the Stratum Corneum

Intercellular diffusion through the stratum corneum is modeled as a three-phase continuum. The keratinized cells in the stratum corneum are considered to be an immobile protein phase, which can provide reversible interactions (adsorption and desorption) with chemicals in the mobile phases. The mobile phases include the lipid (or oil) and aqueous (water) phases in between the keratinocytes. A differential control volume consisting of these three phases is shown in Figure 3.3.

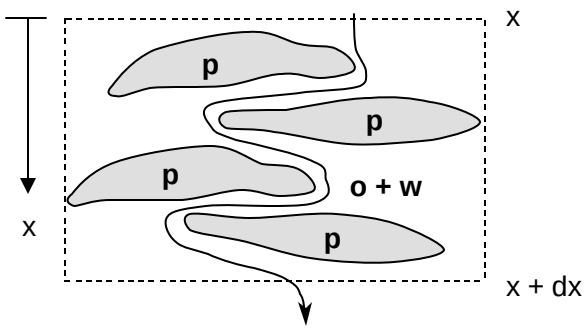

Figure 3.3 Control volume for intercellular chemical diffusion through a three-phase region in the stratum corneum: p = immobile protein phase (keratinocytes), o = mobile oil (lipid) phase, w = mobile water (aqueous) phase.

Assuming that Fick's Law governs the diffusive mass transport through the mobile regions, a one-dimensional mass balance of a chemical diffusing through this three-phase region results in the following partial differential equation for the concentration as a function of time, t [s], and penetration distance into the skin, x [m]:

$$\frac{\partial}{\partial t}\left(C_o f_o + C_w f_w + C_p f_p\right) = \frac{\partial}{\partial x}\left(D_o t_o f_o \frac{\partial C_o}{\partial x} + D_w t_w f_w \frac{\partial C_w}{\partial x}\right) \tag{3.1}$$

where C is the concentration of the chemical present in the phase [kg/m^3-phase]; D_o, D_w, and D_p, are the molecular diffusion coefficients for the oil, water, and protein phases, respectively [m^2/s]; ϕ is the porosity of a given phase [m^3-phase/m^3-total]; t is the tortuosity coefficient (inverse of tortuosity) that expresses the ratio of the linear path length to actual path length; subscript o denotes the oil (or lipid) phase; subscript w denotes the water (or aqueous) phase; and subscript p denotes the protein (or keratinized cell) phase.

We assume that local equilibrium exists and that partitioning between the three phases can be expressed using the following linear relationships:

$$C_o = K_{ow} C_w \tag{3.2}$$

$$C_w = K_{wp} C_p \tag{3.3}$$

$$C_o = K_{op} C_p \tag{3.4}$$

where K is the partitioning coefficient of the phases denoted by the subscripts. Because the protein phase is hydrophilic (Michaels et al., 1975), we also assume that the water-protein partition coefficient is near unity ($K_{wp} = 1$). Therefore, the water and protein concentrations are equivalent (i.e., $C_w = C_p$) and the oil-protein partition coefficient, K_{op}, is equivalent to the oil-water partition coefficient, K_{ow} (often referred to as the octanol-water partition coefficient). The octanol-water partition coefficient is used widely as a measure of polarity in organic chemistry (Flynn, 1990). Using these assumptions, we can then re-write Equation (3.1) in terms of the water concentration as follows:

$$\frac{\partial C_w}{\partial t} = \frac{D_{sc}}{R_{sc}} \frac{\partial^2 C_w}{\partial x^2} \tag{3.5}$$

where $$D_{sc} = D_o t_o f_o K_{ow} + D_w t_w f_w \tag{3.6}$$

$$R_{sc} = K_{ow} f_o + f_w + f_p \tag{3.7}$$

D_{sc} is the effective diffusion coefficient of the three-phase stratum-corneum continuum and R_{sc} is the retardation factor of the three-phase stratum-corneum continuum. The boundary and initial conditions for Equation (3.5**)** are written as follows:

$$C_w(0,t) = C_w^o \tag{3.8}$$

$$C_w(L_{sc},t) = 0 \tag{3.9}$$

$$C_w(x,0) = 0 \tag{3.10}$$

Equation (3.8) assumes that the surface of the stratum corneum is maintained at a constant concentration, C_w^o, in the aqueous phase. Equation (3.9) assumes that at a distance L_{sc} from the surface, capillaries are present that have effectively zero concentration due to a continuous advective flow in the bloodstream (this also assumes that the aqueous region just beneath the stratum corneum in the viable epidermis and dermis does not contribute significantly to the overall resistance of chemical transport). Finally, Equation (3.10) assumes that the initial concentration in the stratum corneum is zero.

The solution to Equations (3.5) to (3.10), which yields the aqueous concentration as a function of time and location in the skin, is presented in Crank (1975, pp. 49-51) and can be written in non-dimensional form as follows:

$$\frac{C_w}{C_w^o} = 1 - \frac{x}{L_{sc}} - \frac{2}{p} \sum_{n=1}^{\infty} \frac{1}{n} \sin \frac{npx}{L_{sc}} e^{-\frac{D_{sc} n^2 p^2 t}{R_{sc} L_{sc}^2}} \tag{3.11}$$

The mass flux into the blood stream (dose), $\dot{m}''$ [kg/m^2-s], can be calculated using Fick's Law at the downstream boundary of the stratum corneum (i.e., $x = L_{sc}$):

$$\dot{m}''_{sc} = -D_{sc} \left. \frac{\partial C_w}{\partial x} \right|_{x=L_{sc}} = \frac{D_{sc} C_w^o}{L_{sc}} \left(1 + 2 \sum_{n=1}^{\infty} (-1)^n e^{-\frac{D_{sc} n^2 p^2 t}{R_{sc} L_{sc}^2}} \right) \tag{3.12}$$

In addition, the cumulative amount of mass (per unit area) diffusing into the blood stream (cumulative dose), Q [kg/m^2], can be expressed as follows:

$$Q_{sc} = \int_0^t \dot{m}''_{sc}\, dt = \frac{D_{sc} C_w^o t}{L_{sc}} - \frac{L_{sc} C_w^o R_{sc}}{6} - \frac{2 L_{sc} C_w^o R_{sc}}{p^2} \sum_{n=1}^{\infty} \frac{(-1)^n}{n^2} e^{-\frac{D_{sc} n^2 p^2 t}{R_{sc} L_{sc}^2}} \tag{3.13}$$

The expressions for both the mass flux, $\dot{m}''_{sc}$, and cumulative dose, Q_{sc}, can be readily non-dimensionalized. Finally, the time required for the system to reach steady-state conditions, t_{sc}^o [s], can be approximated by the following expression adapted from Crank (1975, p. 51):

$$t_{sc}^o \approx 0.45 \frac{L_{sc}^2 R_{sc}}{D_{sc}} \tag{3.14}$$

3.4.2 Diffusion through Sweat Ducts

Chemical permeation through sweat ducts is modeled as a single-phase aqueous diffusion process. A control volume consisting of a sweat duct (or hair follicle) in a larger continuum is shown in Figure 3.4. For simplicity, the region around the sweat duct is assumed to be impermeable (no interactions), and the sweat duct is assumed to be filled with water. The region around the sweat duct is included in the control volume to represent a larger unit area of skin for normalization with the other transport pathways.

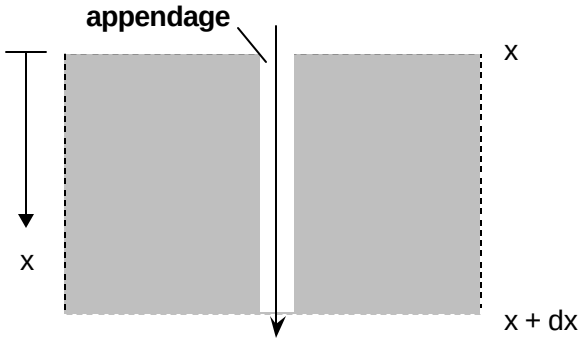

Figure 3.4 Control volume for diffusion through an appendage (sweat duct or hair follicle). Diffusion is assumed to occur through a single-phase fluid in the appendage.

A mass balance of a chemical species diffusing through this control volume can be written as follows:

$$\frac{\partial C_s}{\partial t} = \frac{D_s}{R_s} \frac{\partial^2 C_s}{\partial x^2} \tag{3.15}$$

where

$$D_s = D_w t_s f_s \tag{3.16}$$

$$R_s = f_s \tag{3.17}$$

where the subscript s denotes the sweat duct. Note that the porosity of the sweat duct, f_s, represents the fractional area that the sweat ducts occupy per unit area of skin. It depends on both the density of sweat ducts and the area available for diffusion within each sweat duct. The boundary and initial conditions for Equation (3.15) are the same as those expressed in Equations (3.8) to (3.10) with C_s replacing C_w. The constant aqueous concentration on the surface of the sweat duct is assumed to be the same as the constant aqueous concentration applied to the surface of the skin, C_w^o, in Equation (3.8). In addition, the distance between the surface of the sweat duct and the location where the chemical is carried into the blood stream is denoted as L_s. The solutions for the normalized concentration, the mass flux into the bloodstream, the cumulative mass, and the time to reach steady state are expressed as follows for chemical transport in the sweat duct:

$$\frac{C_s}{C_w^o} = 1 - \frac{x}{L_s} - \frac{2}{p}\sum_{n=1}^{\infty}\frac{1}{n}\sin\frac{npx}{L_s}e^{-\frac{D_s n^2 p^2 t}{R_s L_s^2}} \tag{3.18}$$

$$\dot{m}_s'' = -D_s\left.\frac{\partial C_s}{\partial x}\right|_{x=L_s} = \frac{D_s C_w^o}{L_s}\left(1 + 2\sum_{n=1}^{\infty}(-1)^n e^{-\frac{D_s n^2 p^2 t}{R_s L_s^2}}\right) \tag{3.19}$$

$$Q_s = \frac{D_s C_w^o t}{L_s} - \frac{L_s C_w^o R_s}{6} - \frac{2L_s C_w^o R_s}{p^2}\sum_{n=1}^{\infty}\frac{(-1)^n}{n^2}e^{-\frac{D_s n^2 p^2 t}{R_s L_s^2}} \tag{3.20}$$

$$t_s^o \approx 0.45\frac{L_s^2 R_s}{D_s} \tag{3.21}$$

3.4.3 Diffusion through Hair Follicles

Diffusion through hair follicles is modeled in a similar fashion as diffusion through sweat ducts. The primary difference is that the follicle is assumed to be filled with an oil phase instead of an aqueous phase. Using the control volume shown in Figure 3.4, a mass balance on a chemical species diffusing through the oil phase in the follicle can then be expressed as follows:

$$\frac{\partial C_f}{\partial t} = \frac{D_f}{R_f}\frac{\partial^2 C_f}{\partial x^2} \tag{3.22}$$

where

$$D_f = D_o t_f f_f \tag{3.23}$$

$$R_f = f_f \tag{3.24}$$

where the subscript *f* denotes the hair follicle. The porosity of the hair follicle, f_f, represents the fractional area that the follicles occupy per unit area of skin. It depends on both the density of follicles and the available area for diffusion within each follicle. The boundary condition at the surface of the hair follicle is slightly different than the corresponding boundary conditions of the stratum corneum and sweat duct because the follicle concentration is written in terms of the oil phase. Assuming local equilibrium between the aqueous concentration at the surface boundary of the skin and the concentration in the oil phase at the surface of the follicle, the boundary and initial conditions for the follicle can be written as follows:

$$C_f(0,t) = K_{ow}C_w^o \tag{3.25}$$

$$C_f(L_f,t) = 0 \tag{3.26}$$

$$C_f(x,0) = 0 \tag{3.27}$$

The distance between the surface of the follicle and the location where the chemical is carried into the bloodstream is denoted as L_f. The solutions for the normalized concentration, the mass flux into the bloodstream, the cumulative mass, and the time to reach steady state are expressed as follows for chemical transport in the hair follicle:

$$\frac{C_f}{K_{ow}C_w^o} = 1 - \frac{x}{L_f} - \frac{2}{p}\sum_{n=1}^{\infty}\frac{1}{n}\sin\frac{npx}{L_f}e^{-\frac{D_f n^2 p^2 t}{R_f L_f^2}} \tag{3.28}$$

$$\dot{m}_f'' = -D_f\left.\frac{\partial C_f}{\partial x}\right|_{x=L_f} = \frac{D_f K_{ow}C_w^o}{L_f}\left(1 + 2\sum_{n=1}^{\infty}(-1)^n e^{-\frac{D_f n^2 p^2 t}{R_f L_f^2}}\right) \tag{3.29}$$

$$Q_f = \frac{D_f K_{ow}C_w^o t}{L_f} - \frac{L_f K_{ow}C_w^o R_f}{6} - \frac{2L_f K_{ow}C_w^o R_f}{p^2}\sum_{n=1}^{\infty}\frac{(-1)^n}{n^2}e^{-\frac{D_f n^2 p^2 t}{R_f L_f^2}} \tag{3.30}$$

$$t_f^o \approx 0.45\frac{L_f^2 R_f}{D_f} \tag{3.31}$$

It is important to note that the expressions for the mass flux into the bloodstream in the above solutions use an effective diffusion coefficient preceding the concentration gradient term. The effective diffusion coefficient accounts for the reduced area of the appendages per unit area of skin, as well as the reduced area for diffusion caused by phase interference in the three-phase stratum corneum. However, the coefficient preceding the second derivative in the diffusion equation is expressed by the *ratio* of the effective diffusion coefficient and the retardation factor,

which yields the “diffusivity” for the diffusion equation that appears in the exponent term of the solutions.

3.4.4 Uncertainty Distributions of Input Parameters

The parameters that are used in the solutions presented above can be highly uncertain. As a result, distributions of values are assigned to each of the input parameters using parameter values available in the literature to capture the inherent uncertainty. If insufficient data existed to define a distribution for a parameter, professional judgment was used to assign a distribution for that parameter based on the available values. A Monte Carlo analysis is then performed to obtain a probabilistic distribution of results using the derived solutions. Table 3.1 summarizes the stochastic variables and associated uncertainty distributions that are used in this study.

Table 3.1 Stochastic variables and their uncertainty distributions.

Stochastic Variable	Units	Distribution	Median Value*	Description	Reference
f_o	-	uniform lower bound: 0.15 upper bound: 0.20	0.18	oil-phase porosity in the stratum corneum	1
f_w	-	uniform lower bound: 0.15 upper bound: 0.40	0.27	aqueous-phase porosity in the stratum corneum	1,2
f_p	-	uniform lower bound: 0.35 upper bound: 0.40	0.38	protein-phase porosity in the stratum corneum	1,2
f_s	-	log uniform lower bound: $3.6\text{x}10^{-5}$ upper bound: $8.4\text{x}10^{-3}$	$4.5\text{x}10^{-4}$	fractional area of sweat ducts per unit area of skin (sweat duct porosity)	3
f_f	-	uniform lower bound: $1.5\text{x}10^{-3}$ upper bound: $3.8\text{x}10^{-3}$	$2.8\text{x}10^{-3}$	fractional area of hair follicles per unit area of skin (follicle porosity)	3
t_o	-	log uniform lower bound: 0.01 upper bound: 0.1	0.034	oil-phase tortuosity coefficient in stratum corneum	1
t_w	-	log uniform lower bound: 0.001 upper bound:0.01	$3.1\text{x}10^{-3}$	aqueous-phase tortuosity coefficient in stratum corneum	4
t_s	-	uniform lower bound: 0.1 upper bound: 1.0	0.56	sweat duct tortuosity coefficient	N/A
t_f	-	uniform lower bound: 0.1 upper bound: 1.0	0.52	hair follicle tortuosity coefficient	N/A
D_w	m^2/s	log uniform lower bound: 10^{-10} upper bound: 10^{-9}	$3.2\text{x}10^{-10}$	molecular diffusion coefficient in aqueous phase	5
D_o	m^2/s	log uniform lower bound: 10^{-11} upper bound: 10^{-10}	$3.2\text{x}10^{-11}$	molecular diffusion coefficient in oil phase	6
K_{ow}	-	log normal mean log(K_{ow}): 2.0 st. dev. log(K_{ow}): 1.4	8.8	octanol-water partition coefficient	7
C^o_w	kg/m^3	log uniform lower bound: 0.003 upper bound: 800	2.0	fixed aqueous concentration at the skin surface (aqueous solubility limit)	1,8
L_{sc}	m	log uniform lower bound: $5\text{x}10^{-6}$ upper bound: $6\text{x}10^{-4}$	$5.9\text{x}10^{-5}$	thickness of the stratum corneum	9
L_s	m	uniform lower bound: $2\text{x}10^{-4}$ upper bound: $4\text{x}10^{-4}$	$3.1\text{x}10^{-4}$	length of the sweat duct	1,10
L_f	m	uniform lower bound: $2\text{x}10^{-4}$ upper bound: $4\text{x}10^{-4}$	$3.1\text{x}10^{-4}$	length of hair follicle	1,10

*The median value is calculated from distributions generated by Mathcad®7.
[1]Michaels et al. (1975)
[2]Amsden and Goosen (1995)
[3]Scheuplein (1967)
[4]the aqueous-phase "pores" in the stratum corneum are assumed to have tortuosity-coefficient bounds that are an order of magnitude less than the oil-phase tortuosity coefficient in the stratum corneum
[5] Reid et al. (1987); representative values were taken for solutes diffusing through water
[6]The bounds for the molecular diffusion coefficient in the oil phase are assumed to be an order of magnitude less than the bounds for the aqueous phase
[7]Flynn (1990)
[8]water solubilities of various compounds were used from Michaels et al. (1975)
[9]Scheuplein and Blank (1971)
[10]the distribution is assumed to be equal to the distribution of thicknesses between the skin surface and capillary bed

All of the stochastic input parameters are assumed to be independent. Although one might intuitively expect that the octanol-water partition coefficient, K_{ow}, and aqueous boundary-condition concentration (aqueous solubility), C^o_w, might be correlated, we do not assume any correlation between the input parameters (limited data from Michaels et al. (1975) support this assumption for the oil-water partition coefficient and the water solubility).

3.5 Results and Discussion

Mathcad®7 was used to perform a Monte Carlo analysis of the solutions provided in the previous section. Uncertainty distributions listed in Table 3.1 were developed in Mathcad®7 using a seed value of one, and the corresponding median values are reported in the table. Five hundred realizations were simulated to capture the uncertainty propagated by the sixteen stochastic input variables.

3.5.1 Modeling Results

For brevity, only a subset of the solutions presented in the previous section is used to illustrate the probabilistic analysis. The time required to reach steady-state conditions and the mass flux for each of the penetration routes are examined in detail here. Figure 3.5 shows the distribution of times required to reach steady state for each of the three permeation routes. The median times to reach steady state are 4 minutes, 24 minutes, and 48 minutes for diffusion through the sweat duct, stratum corneum, and hair follicle, respectively. The distributions of steady-state times for transport through the sweat duct and hair follicle each span about two orders of magnitude. The difference between the distributions of steady-state times for the sweat duct and hair follicle is about an order of magnitude, where the sweat duct generally reaches steady state faster. The primary reason for the difference is that the molecular diffusion coefficient for the oil phase in the hair follicle was assumed to be about an order of magnitude less than the molecular diffusion coefficient for water, which comprises the sweat ducts. The results for the stratum corneum span nearly five orders of magnitude. The effective diffusion coefficient for the three-phase stratum corneum depends on a number of additional stochastic parameters that contribute additional uncertainty to the results.

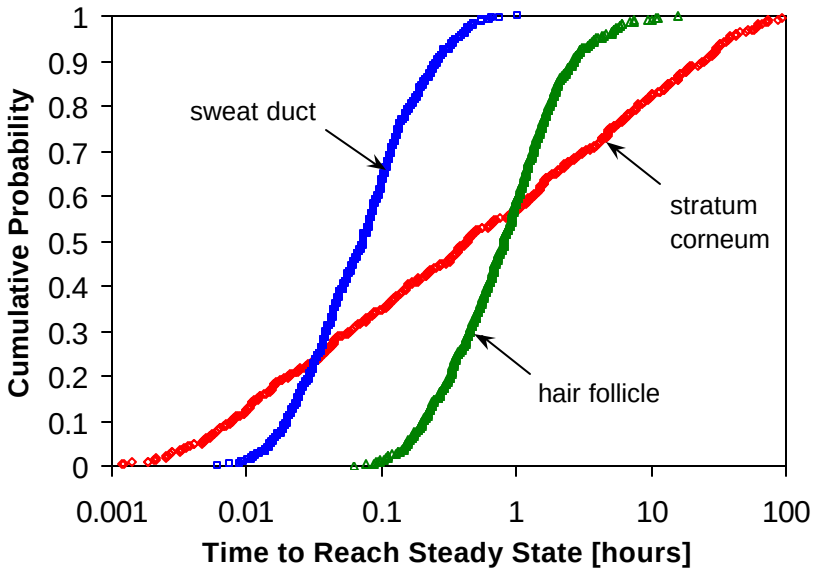

Figure 3.5 Cumulative probability distribution of times required to reach steady state for chemical diffusion through three permeation routes of the skin using 500 realizations.

The mass flux into the bloodstream for each of the three permeation routes is calculated at two different times: 60 seconds and 1 hour. At 60 seconds (~0.02 hours), Figure 3.5 shows that most of the realizations for each permeation route are still in an early transient state; at 1 hour, most of the realizations (> 50%) for each of the permeation routes have reached a steady-state condition. By evaluating the mass flux into the bloodstream at these two times, we intend to glean information regarding the most important pathways and parameters during both early-time transient diffusion as well as long-term diffusion when the pathways are approaching steady state.

Figure 3.6 shows the cumulative distribution function for the mass flux into the bloodstream, $\dot{m}''$, for each of the three permeation routes at 60 seconds. The units of mass flux used in the plot are nanograms per square centimeter per hour [ng/cm^2-h] where 1 ng = 10^{-9} g. At this early transient time period, many of the realizations for diffusion through the hair follicle and stratum corneum result in negligible mass flux at the lower boundary (bloodstream) of the modeled domain; however, the spread in results is significant, and values reach as high as 10^4 and 10^8 ng/cm^2-h for the hair follicle and stratum corneum, respectively. For most of the realizations at this early time, the mass flux through the sweat duct is greatest. The median mass flux into the bloodstream from the sweat duct is 17 ng/cm^2-h, whereas the median mass fluxes from the hair follicle and stratum corneum are 10^{-9} and 0.02 ng/cm^2-h, respectively.

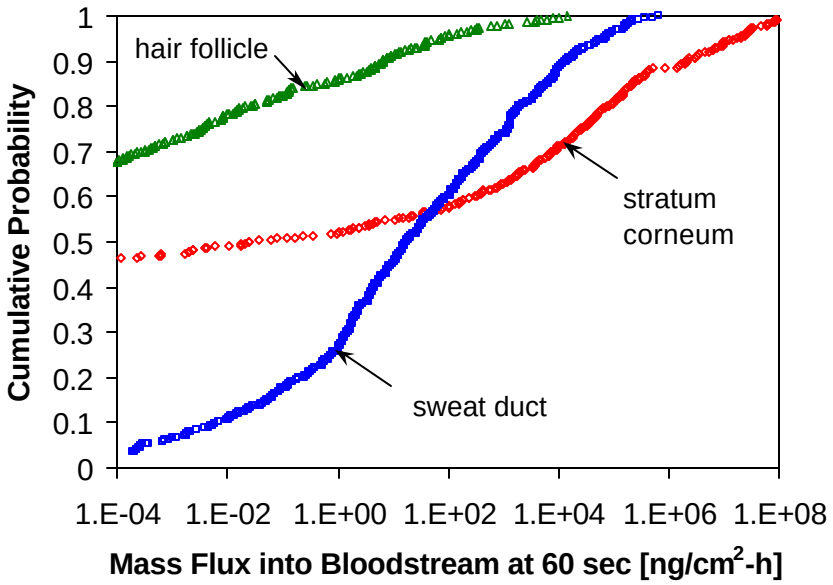

Figure 3.6 Cumulative probability distribution of mass flux into the bloodstream at 60 seconds for chemical diffusion through three permeation routes of the skin using 500 realizations.

Figure 3.7 shows the cumulative distribution function for the mass flux into the bloodstream, $\dot{m}''$, at 1 hour. At 1 hour, many of the realizations have reached steady state (see Figure 3.5), and the spread in mass-flux values is significantly reduced for each of the three permeation routes. The distribution of results for the three-phase stratum corneum exhibits the most uncertainty, primarily because the model relies on the largest number of stochastic variables compared to the other permeation routes. In general, the mass flux into the bloodstream at 1 hour is greatest in the stratum corneum, followed by the mass flux from the hair follicle and sweat duct. The median mass fluxes into the bloodstream from the sweat duct, hair follicle, and stratum corneum are 190, 560, and 8900 ng/cm^2-h, respectively. Recall that the mass flux into the bloodstream from the hair follicle at early times was significantly less than the mass flux from the sweat duct because of the lower molecular diffusion coefficient in the oil phase of the hair follicle. However, the fractional area of hair follicles per unit area of skin is significantly greater than the fractional area of sweat ducts (see Table 3.1). Therefore, after an hour (when sufficient time had elapsed for steady-state conditions to be approached), the larger fractional area of hair follicles allowed more mass to diffuse into the bloodstream per unit area of skin. Similarly, as steady-state diffusion was approached in the stratum corneum at 1 hour, the large surface area allowed relatively more mass to diffuse into the bloodstream. At later times, when more of the realizations would achieve steady state in the stratum corneum, we would expect that the mass flux in the bloodstream would be dominated by the stratum corneum.

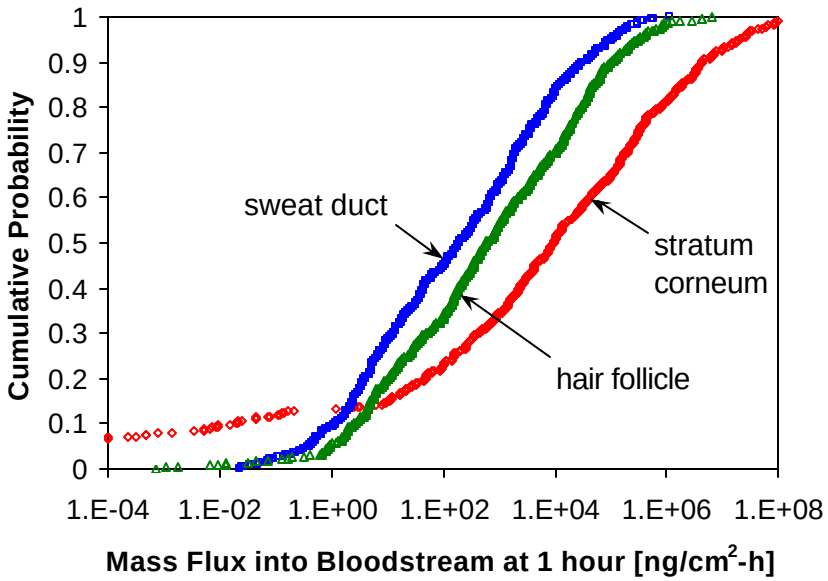

Figure 3.7 Cumulative probability distribution of mass flux into the bloodstream at 1 hour for chemical diffusion through three permeation routes of the skin using 500 realizations.

Finally, the distributions of total mass flux into the bloodstream from the three permeation routes at 60 seconds and 1 hour are plotted in Figure 3.8. The median mass fluxes at 60 seconds and 1 hour are 1.3×10^3 and 2.4×10^4 ng/cm^2-h, respectively. The uncertainty is reduced at 1 hour relative to at 60 seconds because as time progresses and steady-state conditions are approached, the solutions depend on fewer stochastic parameters. It is interesting to compare the resulting distributions with required dosages of various drugs reported in the literature. Amsden and Goosen (1995) report that the required adult dosage for various peptides can range from 2-4 micrograms per day for vasopressin (an antidiuretic hormone that regulates the excretion of body water through urine) to ~3,000 micrograms per day for insulin (a hormone used to convert sugar to energy). Assuming that a transdermal patch covers approximately 10 cm^2 of skin, the required average mass flux into the bloodstream would be approximately 13 ng/cm^2-h for vasopressin and 1.3×10^4 ng/cm^2-h for insulin. Figure 3.8 shows that the probabilities of obtaining the required mass fluxes for vasopressin and insulin at 60 seconds after application of the transdermal patch is about 75% and 35%, respectively, using the assumed input distributions in this model. At 1 hour, the probabilities increase to 95% and 55%, respectively. It is important to note, however, that the values derived in this model are based on general input values that are intended to capture a large range of uncertainty for percutaneous absorption. Using properties specific to these two drugs (e.g., water solubility, partition coefficients, etc.) in the model will likely change the results.

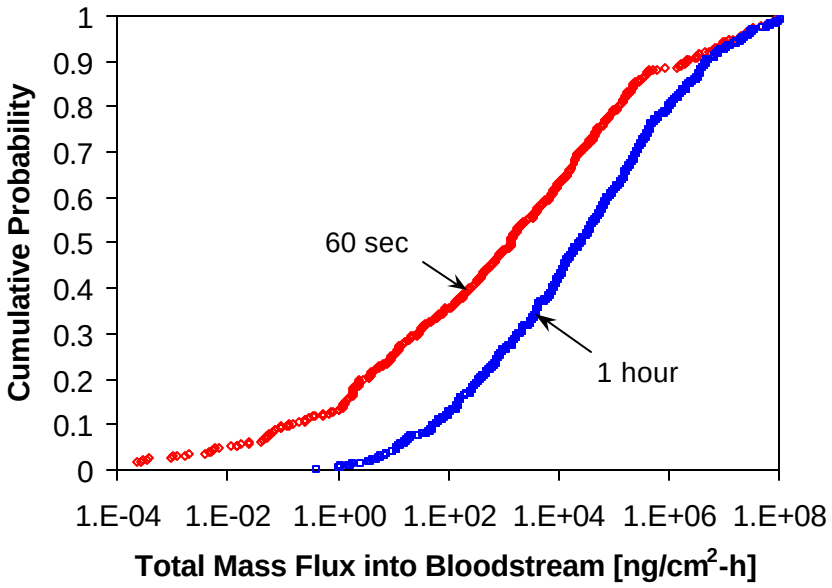

Figure 3.8 Cumulative probability distribution of total mass flux into the bloodstream (sum of stratum corneum, sweat duct, and hair follicle) at 60 seconds and 1 hour using 500 realizations.

3.5.2 Sensitivity Analyses

Analyses can be performed to determine the sensitivity of the dependent variables (e.g., mass flux into the bloodstream) to the stochastic independent variables (e.g., thickness of the stratum corneum, length of the sweat duct, etc.). A stepwise linear regression is a modified version of multiple regression that selectively adds input parameters (independent variables) to the regression model in successive steps. The stepwise process continues until no more variables with a significant effect on the dependent variable are found. The order of parameter selection for incorporation into the regression model gives an indication of their relative importance. The change in the coefficient of determination (ΔR^2) for a given step indicates the fraction of the variance in the model output explained by the input parameter added in that step.

In order to implement a linear regression, a rank transformation (assigning the smallest value of a given variable a value of 1, the next largest value of a given variable a value of 2, and so on) of independent and dependent variables is required and is generally used to compensate for potential non-linear relationships in the stepwise linear regression method for complex model results. Rank transformation essentially allows regression on the strength of the monotonic relationship, instead of the strength of the linear relationship between independent and dependent variables. This stepwise linear regression method provides insight into the relationship between uncertainty in input parameters and the uncertainty in modeling results for complex probabilistic models. In addition, this method provides a quantitative basis for prioritizing the importance of relevant input parameters and processes.

A stepwise linear-regression analysis was performed using Statistica 6.0 on the results of the total mass flux into the bloodstream at 60 seconds and 1 hour (Figure 3.8 shows the results of the simulated total mass flux). Table 3.2 lists the key parameters that were identified at 60 seconds and 1 hour and their corresponding incremental contributions (ΔR^2) to the coefficients of determination (R^2). Also shown are the semi-partial correlations for each parameter. The semi-partial correlation is a measure of the proportion of (unique) variance accounted for by the parameter relative to the total variance of the output variable after controlling for the other input parameters. The semi-partial correlation is similar to the incremental coefficients of determination, but the sign of the semi-partial correlation indicates whether the correlation is positive or negative. Parameters with incremental coefficients of determination greater than 0.005 are presented.

Table 3.2 Summary of parameters important to the simulated total mass flux into the bloodstream at two different times based on stepwise linear-regression analysis. See Table 3.1 for a list of all input parameters and their distributions.

Step	Variable	R^2	ΔR^2	Semi-Partial Correlation
60 Seconds				
1	aqueous solubility limit	0.382	0.382	0.608
2	thickness of stratum corneum	0.701	0.319	-0.581
3	aqueous molecular diff. coefficient	0.727	0.026	0.172
4	sweat-duct porosity	0.751	0.024	0.151
5	sweat-duct tortuosity coefficient	0.770	0.019	0.131
6	oil molecular diffusion coefficient	0.786	0.016	0.121
7	octanol-water partition coefficient	0.800	0.014	0.113
8	oil tortuosity coefficient	0.807	0.007	0.087
1 Hour				
1	aqueous solubility limit	0.747	0.747	0.846
2	thickness of stratum corneum	0.875	0.128	-0.376
3	octanol-water partition coefficient	0.919	0.045	0.203
4	oil molecular diffusion coefficient	0.939	0.019	0.131
5	oil tortuosity coefficient	0.948	0.009	0.103

At 60 seconds, the total mass flux is most sensitive to the aqueous solubility limit, C^o_w, which was used as the upper boundary condition for the concentration in the skin. Based on the incremental coefficient of determination, this parameter accounts for 38% of the variability in the results, with larger values resulting in larger mass fluxes. The thickness of the stratum corneum is also important, with nearly 32% of the variability in the simulated mass flux explained by this parameter. As indicated by the negative sign of the semi-partial correlation for this parameter, there is an inverse relationship between the thickness of the stratum corneum and the simulated total mass flux into the bloodstream (i.e., the thicker the stratum corneum, the lower the mass flux). The aqueous molecular diffusion coefficient and parameters associated with the sweat duct are the next most important parameters, followed by the oil-phase molecular diffusion coefficient, the octanol-water partition coefficient, and the oil-phase tortuosity coefficient. In

total, 81% of the variability in the output is explained using the multiple regression model with these 8 key parameters (the top five or six parameters could be used with nearly the same confidence).

At 1 hour, nearly 95% of the total variability in the simulated mass flux into the bloodstream can be explained by five key parameters. The two most important parameters are the aqueous solubility and the thickness of the stratum corneum, similar to the results at 60 seconds. However, the next three most important parameters are associated with transport through the oil phase in the hair follicle. As explained earlier, at 1 hour, more realizations have reached steady state, and the larger number of hair follicles (follicle porosity) relative to the number of sweat ducts (sweat duct porosity) allows a greater simulated mass flux into the bloodstream when compared to earlier transient times when many of the realizations had not yet allowed mass to reach the bottom boundary.

Figure 3.9 provides a graphical interpretation of the results of the stepwise linear regression using the simulated total mass flux into the bloodstream as the dependent variable. It should be noted that although the results show the strongest sensitivity to aqueous solubility limit, which was used as the aqueous-phase skin concentration at the upper boundary of the simulated domains, the distribution assigned to this parameter in Table 3.1 spans over five orders of magnitude. The range was taken from a variety of chemicals that were reported in the literature to capture the full uncertainty distribution for various chemicals. If the chemical of interest is prescribed or known, this parameter (or an analogous form of it, i.e., the vehicle-tissue partition coefficient per Scheuplein, 1976) will likely exhibit a much smaller range of uncertainty. The resulting sensitivity to this parameter, while still significant, may therefore be reduced if the chemical is prescribed a priori.

Another note of interest regarding the sensitivity analysis is that the molecular diffusion coefficients for water and oil depend on a number of additional parameters such as the molecular weight of the diffusing species, temperature, viscosity, etc. The molecular weight (or molecular volume) of a chemical has been identified as an important parameter impacting percutaneous absorption (Flynn, 1990; Potts and Guy, 1995). If a functional relationship between the molecular diffusion coefficient and these parameters had been used (see, for example, Reid et al., 1987), uncertainty distributions could have been assigned to these additional parameters in lieu of the diffusion coefficient to identify the relative importance of these parameters on percutaneous absorption.

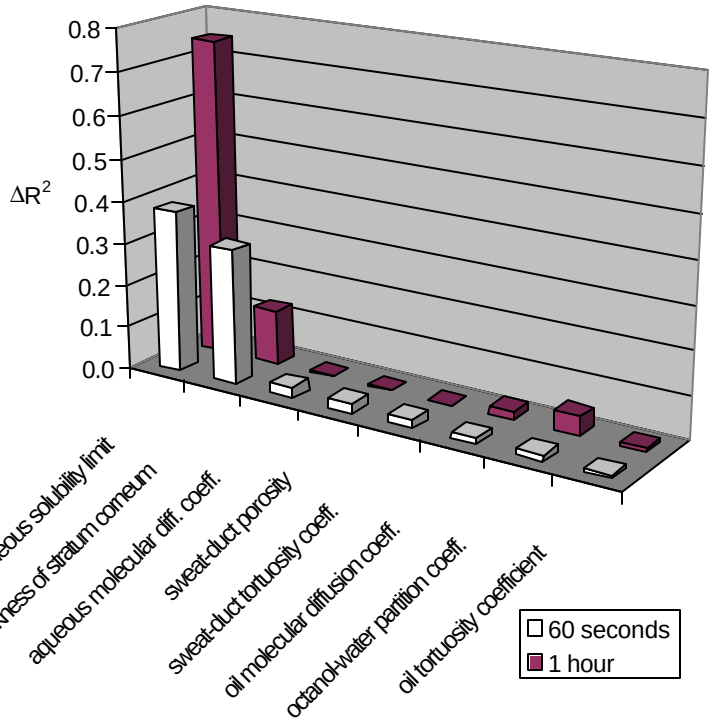

Figure 3.9 Results of stepwise linear regression analysis showing the dependence of the total mass flux (sum of mass flux through stratum corneum, sweat duct, and hair follicle) on key independent stochastic parameters at two different times.

3.5.3 Discussion

The foregoing analyses and results have illustrated significant features and benefits of a probabilistic assessment of percutaneous absorption. In particular, the ability to quantify the uncertainty associated with a specific model and to identify the parameters most important to the simulated results can benefit studies ranging from exposure assessments to transdermal drug delivery.

3.5.3.1 Implications for Exposure Assessment

The United States Environmental Protection Agency produced a comprehensive report describing the principals and applications of dermal exposure assessment (EPA, 1992). The report summarizes the mechanisms of dermal absorption, techniques for measuring dermal absorption, and mathematical models available at the time for dermal absorption and risk assessment. The purpose of this report was to provide exposure assessors with the knowledge and tools required to evaluate dose and subsequent health risks associated with dermal exposure at waste disposal sites or contaminated soils where contaminants could reside in soil, air, and water. The report stated that exposure and risk assessment associated with dermal contact remains the least well understood of the major exposure routes (relative to ingestion and inhalation) because considerable uncertainty exists in parameters and processes associated with dermal absorption. Strangely, all of the mechanistic models presented in the report are

deterministic in nature; none of them provide a quantification of uncertainty or sensitivity analyses of the mechanisms and parameters associated with percutaneous absorption. We believe that the use of probabilistic analyses that incorporate inherent uncertainty in the model parameters and processes will yield more useful and meaningful results when determining and reporting health risks associated with dermal absorption.

3.5.3.2 Implications for Transdermal Drug Delivery

One of the significant problems of transdermal drug delivery is the ability to deliver sufficient doses of a particular drug through the skin. Several methods have been developed to augment the passive diffusion of water-soluble drugs such as peptides and proteins through the skin (Amsden and Goosen, 1995), and these are briefly summarized below:

- *Prodrugs*: Lipophilic groups are covalently bonded onto functional groups of the drug to improve partitioning into the intercellular lipid lamellae of the stratum corneum. Enzymes detach the lipophilic groups *in vivo*, rendering them free and active. However, prodrugs have molecular size restrictions and require synthesis.

- *Chemical permeation enhancers*: Compounds exist that alter the skin as a permeability barrier. Known permeation enhancers include solvents and surfactants; however, the physical basis for the method of enhancement is still unknown. No general theory of chemical enhancement has been provided.

- *Iontophoresis*: An iontophoretic device consists of two electrodes immersed in an electrolyte solution and placed on the skin. When an electric current is applied across the electrodes, an electric field is created across the stratum corneum that drives the delivery of ionized drugs. The primary route of ion transport appears to be through hair follicles or sweat glands, although additional uncertain pathways may be created. This method is restricted to short-term delivery.

- *Electroporation*: Electroporation involves the application of high-voltage electric pulses to increase the permeation through lipid bilayers. This differs from iontophoresis in the duration and intensity of the application of electrical current (iontophoresis uses a relatively constant low-voltage electric field). The high-voltage electric pulse of electroporation is believed to induce a reversible formation of hydrophilic pores in the lipid lamellae membranes that can provide a high degree of permeation enhancement, but the physics and dynamics of this process are not completely understood. This method is restricted to short-term delivery.

- *Ultrasound*: Ultrasound applies sound waves having a frequency greater than 16 kHz to the skin, which causes compression and expansion of the tissue through which the sound waves travel. The resulting pressure variations cause a number of processes (e.g., cavitation, mixing, increase in temperature) that may increase the permeation of drugs. Again, the exact processes and physics have not yet been determined, and this method is restricted to short-term delivery.

In all of these methods, significant uncertainty exists regarding the processes and parameters that truly cause enhanced permeation. Probabilistic simulations and sensitivity analyses coupled with mechanistic models of each of these processes can help to identify the most likely processes and parameters that are significant to drug-delivery enhancement. While models of empirical correlations are intended to provide similar information, they are not inherently based on physical processes or mechanisms. If processes or parameters are introduced that have not been used in these correlations, the results are likely to be erroneous. Therefore, mechanistic models combined with probabilistic analyses are needed to better understand and improve these methods.

3.5.3.3 Geoscience Analogies

Chemical transport through skin is similar in many ways to chemical transport through geologic media. Both processes involve diffusion and absorption in heterogeneous multiphase media. Figure 3.3 shows that the intercellular pathway for chemical diffusion through the stratum corneum is analogous to diffusion through a porous media containing three phases: (1) an immobile solid phase, (2) a mobile water phase, and (3) a mobile oil phase. Figure 3.4 shows that the permeation route through appendages (sweat ducts and hair follicles) is analogous to transport through fractures or other fast-flow-path features (e.g., root holes, animal burrows, etc.) that exist in a relatively less permeable surrounding geologic media. Complex models of these systems have been developed in the geoscience arena to better understand processes relevant to applications such as enhanced oil recovery, geothermal energy production, subsurface contaminant migration, and environmental remediation.

Numerical simulators used in the oil industry to model three-phase movement of hydrocarbons in the subsurface can probably be applied to models of percutaneous absorption. Advantages of these codes are that they can be applied to transient, multidimensional, non-isothermal, heterogeneous systems. Most of the models used in studies of percutaneous absorption have assumed steady-state, one-dimensional, isothermal, homogeneous systems.

Numerical codes developed to model flow and transport through fractured rock can also be applied to simulations of percutaneous transport through appendages, which act as shunts through the bulk of the skin. Formulations have been developed to include the interactions between fast-flow features and a surrounding low-permeability media (Ho, 1997). These formulations were implemented in "dual-permeability" models that were developed to model flow and chemical transport in fractured rock where interaction between two different permeability materials was important. These dual-permeability models can be used to model the simultaneous transport of chemicals through the bulk stratum corneum as well as through the appendages (hair follicles and sweat ducts). Current models assume that the transport through the appendages and through the stratum corneum are independent.

Finally, constitutive relations developed in the geosciences may be applicable to models of percutaneous transport. For example, numerous studies have been performed to relate parameters such as the effective diffusion coefficient in porous media to parameters such as the tortuosity coefficient and mobile-phase porosity. Processes such as diffusion in porous media

under a thermal gradient have also been investigated in great detail. The use of these studies in trying to better understand processes associated with percutaneous absorption may be extremely beneficial.

3.6 Conclusions

Percutaneous absorption plays an important role in applications dealing with exposure assessment and transdermal drug delivery. Unfortunately, previous models have focused on deterministic, steady-state, homogeneous systems when evaluating chemical transport through the skin. In this study, a transient, three-phase, mechanistic model of percutaneous absorption has been developed. Penetration routes through the skin that were modeled include the following: (1) intercellular diffusion through the stratum corneum comprised of an immobile protein phase and mobile aqueous (water) and oil (lipid) phases; (2) diffusion through aqueous-phase sweat ducts; and (3) diffusion through oil-phase hair follicles. Uncertainty distributions were assigned to model parameters and a probabilistic Monte Carlo analysis was performed to simulate a distribution of mass fluxes through each of the routes. Results indicated that at early times, before steady-state conditions had been established, transport through the sweat ducts provided a significant amount of mass flux into the bloodstream. Because of the uncertainty in the input parameters, a large range of mass fluxes was simulated through each of the three routes at this early time. At longer times (1 hour), when many of the realizations had reached steady state, the uncertainty was reduced, and the relative importance of the pathways had changed. Diffusion through the stratum corneum became important because of the relatively large surface area. Similarly, despite the lower oil-phase molecular diffusion coefficient of the hair follicles, diffusion through the hair follicles was more significant than diffusion through the sweat ducts at later times because of the larger simulated porosity of hair follicles.

Sensitivity analyses were also performed using a stepwise linear regression analysis. Parameters that were most important to the simulated mass flux were identified, and the relative importance of each parameter was quantified through the incremental coefficients of determination and semi-partial correlations. These analyses were found to be extremely useful in not only quantifying the uncertainty in the simulated output variables, but also in identifying the input parameters that were most important to the simulated results. These probabilistic methods can provide more meaningful interpretations of exposure assessments and risk regarding dermal uptake of contaminants. In addition, new methods of enhancing transdermal drug delivery (e.g., ultrasound, electroporation, etc.) have a great deal of uncertainty surrounding the physical processes associated with these methods. Mechanistic models of multiphase, heterogeneous transport through the skin coupled with probabilistic analysis can shed additional insight into how these methods can be improved through identification and refinement of important parameters and processes.

3.7 References

Amsden, B. G. and Goosen, M. F. A. (1995) Transdermal delivery of peptide and protein drugs: an overview. *AIChE Journal*, 41(8), 1972-1997.

Bird, M. G., (1981) Industrial solvents: some factors affecting their passage into and through the skin. *Ann. Occup. Hyg.*, 24(2) 235-244.

Cooper, R. R. (1984) Increased skin permeability for lipophilic molecules. *J. Pharm. Sci.*, 73, 1153.

Crank, J. (1975) *The Mathematics of Diffusion*. 2nd Ed. Oxford University Press, Oxford.

Department of Energy (DOE) (1998) Viability assessment of a repository at Yucca Mountain, Volume 3: Total system performance assessment. *Report DOE/RW-0508/V3*, U.S. Department of Energy, Washington, DC.

Environmental Protection Agency (EPA), (1992) Dermal exposure assessment: principals and applications. Report *EPA/600/8-91/011B*, U.S. Environmental Protection Agency, Washington, DC.

Flynn, G. L. (1990) *Physicochemical Determinants of Skin Absorption*. Published by Elsevier in Proceedings of the Workshop on Principles of Route-to-Route Extrapolation for Risk Assessment, Hilton Head, SC, March 19-21, 93-127.

Ho, C. K. (1997) Models of fracture-matrix interactions during multiphase heat and mass flow in unsaturated fractured porous media. In *Proceedings of the ASME Fluids Engineering Division*, Sixth Symposium on Multiphase Transport in Porous Media, 1997 ASME International Mechanical Engineering Congress and Exposition, FED-Vol. 244, Dallas, TX, November 16-21, pp. 401-412.

Kalia, Y. N. and Guy, R. H. (2001) Modeling transdermal drug release. *Advanced Drug Delivery Reviews*, 48, 159-172.

McDougal, J. N and Boeniger, M. F. (2002) Methods for assessing risks of dermal exposures in the workplace. *Critical Reviews in Toxicology*, 32(4), 291-327.

Michaels, A. S., Chandrasekaran, S. K., and Shaw, J. E. (1975) Drug permeation through human skin: theory and in vitro experimental measurement. *AIChE Journal*, 21(5), 985-1996.

Ness, S. A. (1994) *Surface and Dermal Monitoring for Toxic Exposures*. Van Nostrand Reinhold International Thomson Publishing Company, New York.

Poet, T. S. and McDougal, J. N. (2002) Skin absorption and human risk assessment. *Chemico-biological interactions*, 140, 19-34.

Poet, T. S., Corley, R. A., Thrall, K. D., Edwards, J. A, Tanojo, H., Weitz, K. K., Hui, X., Maibach, H. I., and Wester, R. C. (2000) Assessment of the percutaneous absorption of trichloroethylene in rats and humans using MS/MS real-time breath analysis and physiologically based pharmacokinetic modeling. *Toxicological Sciences*, 56, 61-72.

Potts, R. O. and Guy, R. H. (1995) A predictive algorithm for skin permeability: the effects of molecular size and hydrogen bond activity. *Pharmaceutical Research*, 12(11), 1628-1633.

Reid, R. C., Prausnitz, J. M., and Poling, B. E. (1987) *The Properties of Gases and Liquids*. 4th Ed., McGraw Hill, Inc., New York.

Scheuplein, R. J. (1965) Mechanism of percutaneous absorption I. routes of penetration and the influence of solubility. *J. Investigative Dermatology*, 45(5), 334-346.

Scheuplein, R. J. (1967) Mechanism of percutaneous absorption II. transient diffusion and the relative importance of various routes of skin penetration. *J. Investigative Dermatology*, 48(1), 79-88.

Scheuplein, R. J., (1976) Percutaneous absorption after twenty-five years: or "old wine in new wineskins." *J. Investigative Dermatology*, 61, 31-38.

Scheuplein R. J. and Blank, I. H. (1971) Permeability of the skin. *Physiol. Rev*., 51, 702-747.

Stewart, R. D. and Dodd, H. C. (1964) Absorption of carbon tetrachloride, trichloroethylene, tetrachloroethylene, methylene chloride, and 1, 1, 1-trichloroethane through the human skin. *AIHA Journal*, 25(5), 439-446.

4.0 Crossover Technologies in Geophysics and Biomedical Imaging

Chester J. Weiss

4.1 Introduction

A common goal to both the medical and geoscience communities is to address the problem of developing non-invasive techniques for peering into the interior of an object. Other disciplines share this same objective (such as industrial engineering for quality assurance testing) but for brevity we restrict our discussion to those technologies that are well established in the geosciences (specifically geophysics) and find application as a method for biomedical imaging. Furthermore, we will narrow the expanse of geophysical methods by examining only those that utilize quasi-static electromagnetic fields and electrical impedance estimates for *in situ* characterization of biological structures within the human body. While at the surface this may seem overly restrictive, these methods are still very much in the research development phase in the biomedical imaging community and thus represent areas of professional cross-fertilization between geophysicists and medical imaging specialists.

In short, the problem of imaging an object interior via some non-invasive method can be broadly lumped into two primary steps: measurement of some physical quantity (such as voltage, current, or the electromagnetic fields) on the surface of the body; and utilization of an algorithm which infers the distribution of some physical property (such as electrical conductivity) within the body based solely on these surface measurements. Interpretation of the spatial distribution of physical properties in terms of other meaningful quantities (e.g., Is this area of anomalous electrical conductivity in the image a tumor or benign fatty deposit?) is beyond the scope of this paper but it's worth mentioning that in geophysics and medical imaging alike, the interpretation problem is often based on heuristic arguments which assimilate a variety of complementary datasets and observations.

4.2 Geophysical Imaging Methods

Two imaging methods used by geophysicists for subsurface imaging have recently found utility as methods for imaging the interior of the human body: electrical impedance tomography (EIT) and magnetic induction tomography (MIT). The principles of operation for each method are based on the observation that different biological tissues have varying capacities for sustaining a flow of electric current (Schwan and Takashima, 1993; Jossinet and Lavandier, 1998), and is influenced by, for example, the density of vascularization in a given region. The variations in vascularization can, in some cases, be readily correlated to differences in tissue type such as lung, muscle, and bone tissues in the thorax. In other cases, the variations in the density of vascularization, and hence electrical conductivity, can be attributed to the presence of tumorous growths within the body. Thus, medical imaging by mapping electrical conductivity gives rise to two key applications: monitoring of pulmonary activity (e.g. Metherall, 1998), screening for early cancer detection (Cherpenin et al., 2001; Wang et al., 2001). Other applications of EIT include imaging of human head (Tidswell et al., 2001) and gastrointestinal and esophogeal function (e.g. Devane, 1993; Erol et al., 1995).

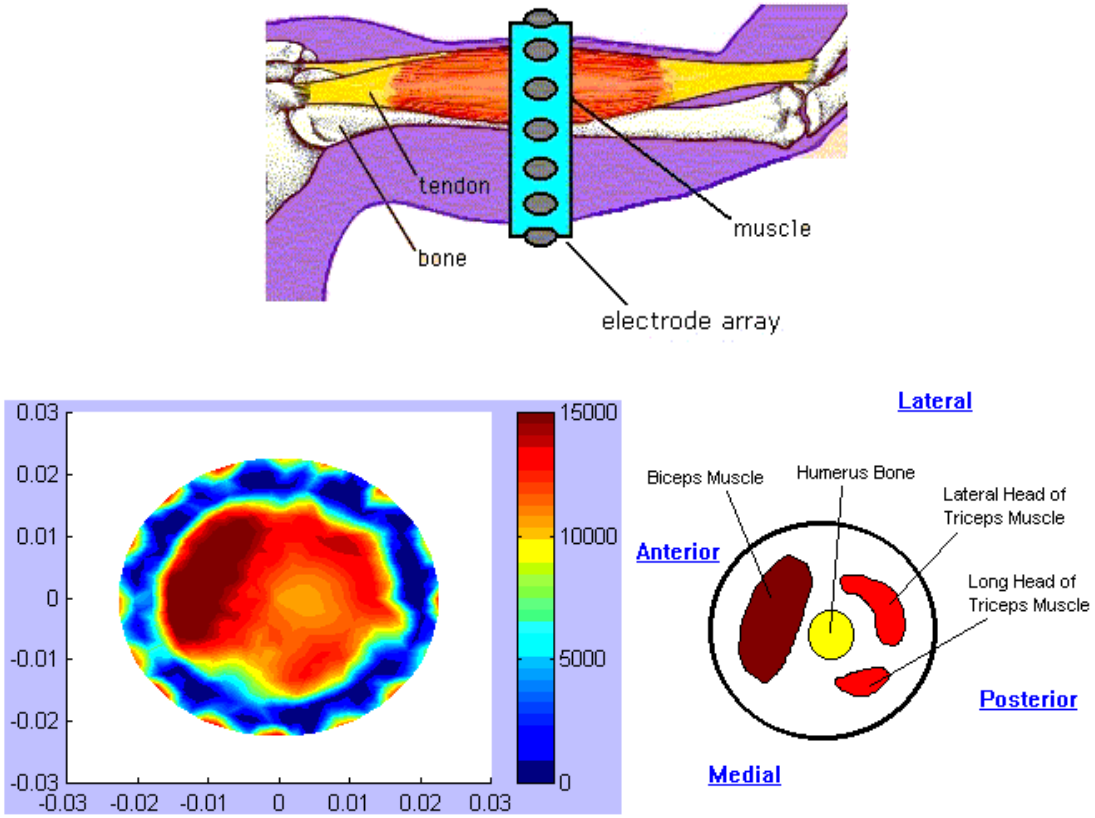

Figure 4.1 Experimental setup (top) for EIT imaging of the upper arm. EIT image of upper arm (lower-left) and interpretation of EIT image (lower-right). Graphics from Dartmouth, Thayer School of Engineering (www-nml.dartmouth.edu/biomedprg/EIS/index.html).

The EIT methods utilize an array of electrodes that are placed in direct electrical contact with the skin. The experiment proceeds as a small amount of electric current is injected into the skin through a pair of electrodes that, in turn, propagates through body and generates a potential difference elsewhere on the skin that can be measured by the other electrodes in the array. Thus, the distribution of measure voltages on the skin is directly affected by the electric current paths generated within the body, and hence, the distribution of electrical conductivity within the body. The method is attractive because data acquisition time is relatively brief (on the order of a few minutes), the electrodes are small and easily attached/removed (Figure 4.1), and the acquisition computer is usually small and portable (Figure 4.2), thus providing an imaging tool which can be used on subjects who have limited physical mobility or are bedridden. Currents are applied with a harmonic time-dependence and typically operate in the frequency range of D.C to 1MHz. If induction is neglected, spatial variation of the measured voltages are dictated by a complex-valued Laplace equation for the electric potential—an equation that is readily solved in 2D/3D by applied mathematicians and geophysicists alike using the usual suite of discrete numerical methods such as finite elements or finite differences (e.g. Molinari et al., 2001).

Figure 4.2 Data acquisition computer for Dartmouth EIT imaging system (www-nml.dartmouth.edu/biomedprg/EIS/index.html).

An example of an experimental setup for the imaging of breast tissues is provided in Figures 4.3 to 4.5. The approach used at Dartmouth University illustrates the ability to discriminate between benign and malignant breast tissues using the EIT method.

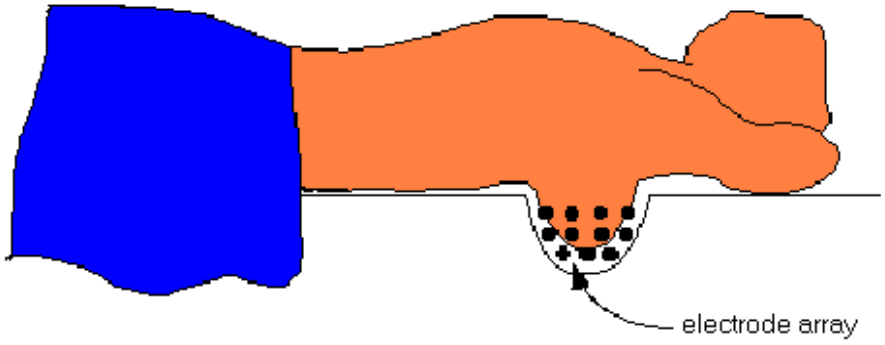

Figure 4.3. Experimental setup for Dartmouth EIT breast cancer imaging system (www-nml.dartmouth.edu/biomedprg/EIS/index.html).

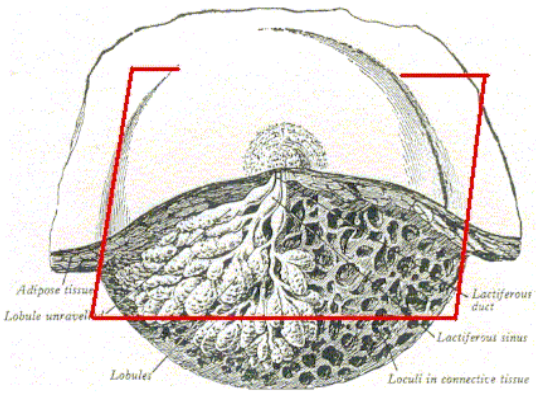

Figure 4.4 Anatomy of a human breast for reference in the EIT images of Figure 4.5 (www-nml.dartmouth.edu/biomedprg/EIS/index.html).

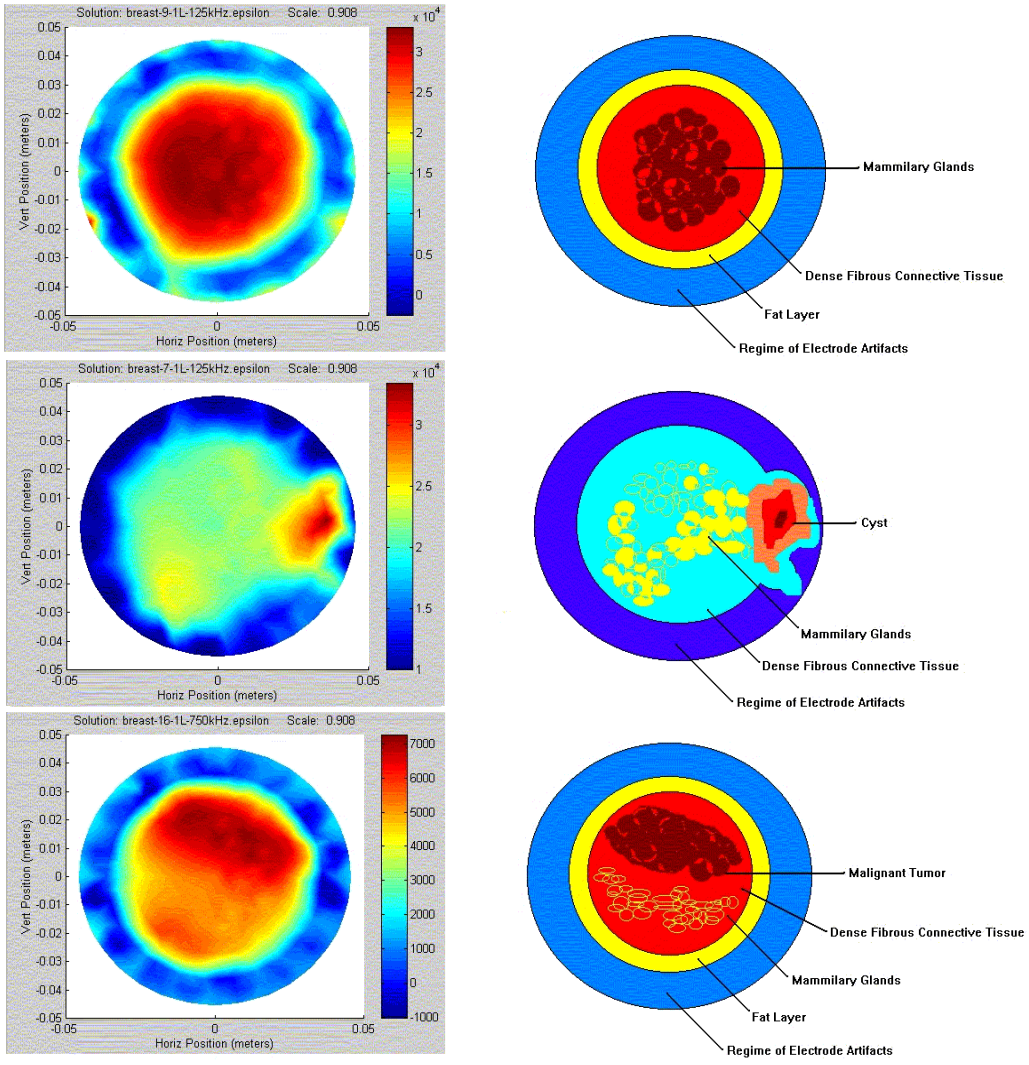

Figure 4.5 EIT images a normal human breast (top), breast with benign cyst (middle) and breast with tumor (bottom) measured using the Dartmouth EIT system. Actual data on is on the left, interpretation of the data is on the right (www-nml.dartmouth.edu/biomedprg/EIS/index.html).

In contrast to the EIT methods, is MIT method (also known as the "induced-EIT" or "touchless" method) works along the same operating principles as the low-frequency induction methods of geophysics whereby an electric current is induced (according to Faraday's Law of Induction) into the electrically conducting body by a nearby antenna loop which is powered by a small time-harmonic electric current. The electrical eddy currents induced in the conducting body therefore also time-harmonic and generated secondary electromagnetic fields that can be measured directly by electrodes (Gencer et al., 1994) or by a separate induction coil (Gencer, 1999). In conjunction with the usual EIT method, the MIT method has the potential to greatly improve the resolution of electrical anomalies within the body since the orientation and location of the transmitting antenna is not constrained to the surface of the skin, but rather, can be located almost arbitrarily above the body and therefore subject the body to a greater variety of EM excitation modes.

Mathematical solution to the EM induction problem in 3D is significantly more challenging than that the EIT problem. In short, the 3D induction problem is characterized by finding solutions of a vector function that obey the complex valued Helmholtz equation: a solution that typically is wrenched out a large, ill-conditioned system of equations (e.g. Newman and Alumbaugh, 1995; Everett and Schultz 1995). For MIT to be practical, the solution to this equation must be available at a minimum of computational cost, a requirement that is presently remedied by so-called `approximate' methods (Gencer et al., 1994). However, the highly non-linear (with respect to electrical conductivity) nature of the governing partial differential equation makes reliance on the approximation methods a risky coarse of action. Instead, rapid and resource-efficient solutions to the fully 3D problem recently appearing in the geophysical literature (e.g. Weiss, 2001; Weiss and Newman, 2002) may find application in the MIT problem.

Solution to the governing equations for both the EIT and MIT problems is a necessary step in any frequentist-based (in contrast to a Bayesian approach) image reconstruction algorithm whereby the image is computed by minimizing the misfit between the predicted and observed data, usually subject to some stabilization or regularization criterion (e.g. Constable et al., 1987). Techniques presently used in the EIT reconstruction problem include linearization of the conductivity term (Mueller et al., 1999), one-step approximate Newton method (Le Hyraic and Pidcock, 2001) and multiple-step Newton method (Edic et al., 1998). Similar strategies are utilized within the geophysics community (e.g. Non-linear conjugate gradients in Newman and Alumbaugh, 2000; Figure 4.6) however the application of other more "exotic" techniques, such as homotopy (Jegen et al., 2001), have yet to appear in the medical imaging literature.

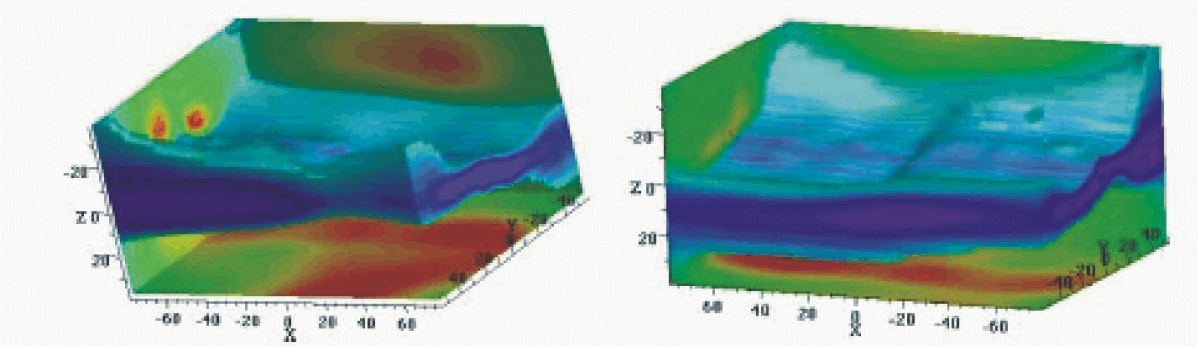

Figure 4.6 Front (left) and back (right) image of a resistive oil-bearing formation in the subsurface reconstructed using a non-linear conjugate gradient inversion of synthetic electromagnetic induction data. Courtesy of G. Newman, Sandia National Laboratories.

4.3 References

Cherepenin V., Karpov, A., Korjenevsky, A., Kornienko, V., Mazaletskaya, A., Mazourov, D., and Meister, D. (2001) A 3D electrical impedance tomography (EIT) system for breast cancer detection. *Physiological Measurement*, 22, 9-18.

Constable, S. C., Parker, R. L., and Constable, C. G. (1987) Occam's inversion: A practical algorithm for generating smooth models from electromagnetic sounding data. *Geophysics*, 52, 289-300.

Devane, S. P. (1993) Application of EIT to gastric emptying in infants: Validation against residual volume method. In D. Holder, Ed., *Clinical and Physiological Application of Electrical Impedance Tomography*. UCL Press, London, 113-123.

Edic, P. M., Isaacson, D., Saulnier, G. L., Jain, H., and Newell, J. C. (1998) A iterative Newton-Raphson method to solve the inverse admittivity problem. *IEEE Transactions, of Biomedical Engineering*, 45, 899-908.

Erol, R. A., Mangnall, R., Leathard, A. C., Smallwood, R. H., Brown, B. H., Cherian, P., and Bardhan, K. D. (1995) Identifying esophogeal contents using electrical impedance tomography. *Physiological Measurement*, *16*, 253-261.

Everett, M. E. and Schultz A. (1995) Electromagnetic induction in eccentrically nested spheres. *Physics of the Earth and Planetary Interiors*, 92, 189-198.

Gencer, N. G., Kuzuoglu, M., and Ider, Y. Z. (1994) Electrical impedance tomography using induced currents. *IEEE Transactions on Medical Imaging*, 13, 338-350.

Gencer, N. G. (1999) Electrical conductivity imaging via contactless measurements. *IEEE Transactions on Medical Imaging*, 18, 617-627.

Jegen, M. D., Everett, M. E., and Schultz, A. (2001) Using homotopy to invert geophysical data. *Geophysics*, 66, 1749-1760.

Jossinet, J. and Lavandier, B. (1998) The discrimination of excised cancerous breast tissue samples using impedance spectroscopy. *Bioelectrochemistry and Bioenergetics*, 45, 161-167.

Le Hyaric, A. and Pidcock, M. K. (2001) A image reconstruction algorithm for three-dimensional electrical impedance tomography. *IEEE Transactions, of Biomedical Engineering*, 48, 230-235.

Metherall, P, (1998) Three dimensional electrical impedance spectroscopy of the human thorax. Ph.D. Thesis, University of Sheffield, U.K.

Molinari, M., Cox, S. J., Blott, B. H., and Baniell, G. J. (2001) Adaptive mesh refinement techniques for electrical impedance tomography. *Physiological Measurement*, 22, 91-96.

Mueller, J. L., Isaacson, D., and Newell, J. C. (1999) A reconstruction algorithm for electrical impedance tomography data collected on rectangular arrays. *IEEE Transactions, of Biomedical Engineering*, 46, 1379-1386.

Newman, G. A. and Alumbaugh, D. L. (1995) Frequency-domain modelling of airborne electromagnetic responses using staggered finite differences. *Geophysical Prospecting*, 43, 1021-1042.

Newman, G. A. and Alumbaugh, D. L. (2000) Three-dimensional magnetotelluric inversion using non-linear conjugate gradients. *Geophysical Journal International*, 140, 410-424.

Schwan, H. P. and Takashima, S. (1993) Electrical conduction and dielectric behavior in biological systems. *Encyclopedia of Applied Physics*, VHC Publishers, New York, 177-200.

Tidswell, A. T., Gibson, A., Bayford, R. H., and Holder, D. S. (2001) Validation of a 3D reconstruction algorithm for EIT of human brain function in a realistic head-shaped tank. *Physiological Measurement*, 22, 177-185.

Wang, W., Tang, M., McCormick, M., and Dong, X. (2001) Preliminary results from an EIT breast imaging simulation system. *Physiological Measurement*, 22, 39-48.

Weiss, C. J. (2001) A matrix--free approach to solving the fully 3D electromagnetic induction problem, 3-D anisotropic Earth. *71st Annual Meeting of the Society of Exploration Geophysicists*, San Antonio TX.

Weiss, C. J. and Newman, G. A. (2002) A fast preconditioner for the electromagnetic induction problem in 3D anisotropic media. *Geophysics*, in press.

Distribution

1	MS 0188	M. L. Garcia, 1030
1	MS 0188	C. E. Meyers, 1030
1	MS 0316	S. J. Plimpton, 9209
1	MS 0316	S. S. Dosanjh, 9233
1	MS 0316	J. B. Aidun, 9235
1	MS 0318	P. Yarrington, 9230
1	MS 0321	W. J. Camp, 9200
1	MS 0511	J. C. Cummings, 1000
1	MS 0513	A. D. Romig, 1000
1	MS 0701	W. R. Cieslak, 6100
1	MS 0701	P. B. Davies, 6100
1	MS 0724	R. J. Eagan, 6000
10	MS 0735	C. K. Ho, 6115
1	MS 0735	E. K. Webb, 6115
1	MS 0741	M. L. Tatro, 6200
1	MS 0750	L. C. Bartel, 6116
1	MS 0750	G. A. Newman, 6116
1	MS 0750	M. C. Walck, 6116
10	MS 0750	C. J. Weiss, 6116
1	MS 0750	L. J. Criscenti, 6118
10	MS 0750	R. T. Cygan, 6118
10	MS 0750	H. R. Westrich, 6118
1	MS 0751	L. S. Costin, 6117
1	MS 0819	E. A. Boucheron, 9231
1	MS 0820	P. F. Chavez, 9232
1	MS 0824	A. C. Ratzel, 9110
1	MS 0834	J. E. Johannes, 9114
1	MS 0835	M. J. McGlaun, 9140
1	MS 0841	T. C. Bickel, 9100
1	MS 0885	D. B. Dimos, 1801
1	MS 0885	G. S. Heffelfinger, 1802
1	MS 0887	M. J. Cieslak, 1800
1	MS 0888	R. L. Clough, 1811
1	MS 0889	J. W. Braithwaite, 1832
1	MS 1079	M. W. Scott, 1700
1	MS 1089	G. L. Peace, 6135
1	MS 1110	D. E. Womble, 9214
1	MS 1349	W. F. Hammetter, 1843
1	MS 1373	R. M. Salerno, 5324
1	MS 1411	E. H. Fang, 1834
1	MS 1411	B. G. Potter, 1846
1	MS 1413	T. A. Michalske, 1040
1	MS 1413	B. C. Bunker, 1141

Distribution (continued)

1	MS 1413	J. Liu, 1141
1	MS 1415	J. C. Barbour, 1112
1	MS 1415	N. D. Shinn, 1114
1	MS 1421	G. A. Samara, 1120
1	MS 1425	S. J. Martin, 1707
1	MS 1425	M. S. Derzon, 1740
1	MS 1425	S. A. Casalnuovo, 1744
1	MS 1425	R. C. Hughes, 1744
1	MS 1427	J. M. Phillips, 1100
1	MS 1413	G. D. Bachand, 1141
1	MS 1413	A. R. Burns, 1141
1	MS 1413	P. V. Dressendorfer, 1141
1	MS 1413	D. Y. Sasaki, 1141
1	MS 9004	J. Vitko, 8100
1	MS 9054	W. J. McLean, 8300
1	MS 9054	R. W. Carling, 8350
1	MS 9104	W. R. Bolton, 8120
1	MS 9161	E. Chen, 8726
1	MS 9201	P. K. Falcone, 8114
1	MS 9405	R. H. Stulen, 8700
1	MS 9951	L. M. Napolitano, 8100
1	MS 9018	Central Technical Files, 8945-1
2	MS 0899	Technical Library, 9616
1	MS 0612	Review and Approval Desk, 9612 For DOE/OSTI